A Thesis for the Degree of Doctor of Philosophy

Structural and functional studies of inulin fructotransferase and phytotoxin toxoflavin-degrading enzyme

이눌린 분해효소와 식물독소 톡소플라빈 분해효소의 3 차 구조 규명과 생화학적 기능 연구

February 2014

Department of Agricultural Biotechnology
Seoul National University

Woo-Suk Jung

이눌린 분해효소와 식물독소 톡소플라빈 분해효소의 3차 구조 규명과 생화학적 기능 연구

Structural and Functional Studies of Inulin Fructotransferase and Phytotoxin Toxoflavin-degrading Enzyme

지도교수 : 이 상 기

이 논문을 농학박사학위논문으로 제출함
2014년 1월

서울대학교 대학원
농생명공학부 응용생명화학전공
정 우 석

정우석의 박사학위논문을 인준함
2014년 1월

위 원 장 _____ 인

부위원장 _____ 인

위 원 _____ 인

위 원 _____ 인

위 원 _____ 인

Structural and Functional Studies of Inulin Fructotransferase and Phytotoxin Toxoflavin-degrading Enzyme

ADVISOR : Sangkee Rhee

A Dissertation Submitted in Partial Fulfillment
of the Requirement for the Degree of

DOCTOR OF PHILOSOPHY

to the Faculty of
Department of Agricultural Biotechnology
at

SEOUL NATIONAL UNIVERSITY

by

Woo-Suk Jung

Date Approved

_____ _____

_____

_____

_____

_____

ABSTRACTS

Inulin fructotransferase (IFTase), a member of glycoside hydrolase family 91, catalyzes a depolymerization of β-2,1-fructans inulin by successively removing the terminal difructosaccharide units as cyclic anhydrides *via* intramolecular fructosyl transfer. The crystal structures of IFTase and its substrate-bound complex reveal that IFTase is a trimeric enzyme, and each monomer folds into a right-handed parallel β-helix. Despite variation in the number and conformation of its β-strands, the IFTase β-helix has a structure that is largely reminiscent of other β-helix structures, but is unprecedented in that trimerization is a prerequisite for catalytic activity and the active site is located at the monomer-monomer interface. Results from crystallographic studies and site-directed mutagenesis provide a structural basis for the exolytic-type activity of IFTase, and a functional resemblance to inverting-type glycosyltransferases.

Pathogenic bacteria synthesize and secrete toxic low molecular weight compounds as virulence factors, which play essential roles in the pathogenicity of bacteria in various hosts. Therefore, these chemicals are targets for antivirulence strategies. The phytopathogen *Burkholderia glumae* BGR1 produces a phytotoxin, toxoflavin, which is the key factor in bacterial wilting

of crop plants. Recently, toxoflavin-degrading enzyme (TxDE) was identified from *Paenibacillus polymyxa JH2*. Here, the crystal structure of TxDE in the substrate-free form at 1.6 Å resolution and in complex with toxoflavin at 2.0 Å resolution is reported along with the results of a functional analysis. The overall structure of TxDE is similar to the structures of the vicinal oxygen chelate superfamily of metalloenzymes, despite the lack of apparent sequence identity. The active site is located at the end of the hydrophobic channel, 9 Å in length, and contains a Mn(II) ion interacting with one histidine residue, two glutamate residues, and three water molecules in an octahedral coordination. The binding of substrate did not cause any noticeable conformational changes in the enzyme, and toxoflavin binds in the Mn(II)-coordination shell by replacing ligating water molecules. A functional analysis indicated that TxDE catalyzes the degradation of toxoflavin in a manner dependent on oxygen, Mn(II), and the reducing agent dithiothreitol (DTT). These results provide insight into the catalytic mechanism of TxDE, its recently proposed role as a non-antibiotic selection marker for plants, and its function as an antivirulence factor in toxoflavin-mediated plant diseases.

Keyword ; crystal structure, fructan, Inulin fructotransferase, difructose anhydride, right-handed β-helix, inverting-type glycosyltransferase, phytotoxin, *Burkholderia glumae*, *Paenibacillus polymyxa JH2*, Toxoflavin-degrading enzyme, βαβββ-motif, metalloenzyme.

Student Number; 2004-31068

CONTENTS

CHAPTER II. Structural and Functional Analysis of Phytotoxin Toxoflavin-Degrading Enzyme

LIST OF FIGURES

CHAPTER I

CHAPTER II

LIST OF TABLES

CHAPTER I

CHAPTER II

LIST OF ABBRIVIATIONS

AHL	*N*-acylhomoserine lactone
CAPS	3-(Cyclohexylamino)-1-propanesulfonic acid
CAZy	Carbohydrate-Active enZymes
CbhA	Cellobiohydrase
CCP4	Collaborative Computational Project Number 4
CNS	Crystallography & NMR System
DFA	Difructose anhydride
DHBD	2,3-Dihyroxybiphenyl 1,2-dioxygenase
DTD	1,2-Dithiane-4,5-diol
DTT	Dithiothreitol
EDTA	Ethylenediaminetetraacetic acid
GH	*O*-Glycoside hydrolase
HEPES	4-(2-Hydroxyethyl)piperazine-1-ethanesulfonic acid
IFTase	Inulin fructotransferase
IPTG	Isopropyl β-$_D$-1-thiogalactopyranoside
LC-MS	Liquid Chromatography-Mass Spectrometry
MAD	Multiwavelength anomalous diffraction
MES	2-(*N*-Morpholino)ethanesulfonic acid
NCS	Non-crystallographic symmetry
NMR	Nuclear Magnetic Resonance
LFTase	Levan fructotransferase

PCR	Polymerase chain reaction
PEG	Polyethylene glycol
PEGMME	Polyethylene glycol monomethyl ether
PelC	Pectate lyase C
rmsd	Root-mean-square deviation
SDS-PAGE	Sodium dodecyl sulfate-Polyacrylamide gel electrophoresis
SeMet	Seleno-methionine
TLC	Thin-layer chromatography
Tris	Trizma® base
TSP	Phase P22 tailspike protein
TxDE	Toxoflavin-degrading enzyme
UV	Ultraviolet

CHAPTER I

Structural and Functional Insights into Intramolecular Fructosyl Transfer by Inulin Fructotransferase

INTRODUCTION

Fructans are polysaccharides composed of linear and branched polymers of fructose linked to sucrose through glycosidic bonds of various linkage types. They have been conceived as one of the principal stored forms of energy in 15% of higher plants, as well as in a wide range of bacteria and fungi (Vijin and Smeekens 1999). Several plant fructosyltransferases, each with a distinct substrate and glycosidic bond linkage-type specificity, have been suggested to be involved in the sequential enzymatic steps that produce fructans such as β-2,6-linked levan and β-2,1-linked inulin. In this process, fructose is first linked to vacuolar sucrose, and then fructosyl units are successively added to the resulting trisaccharide (Vijin and Smeekens 1999; Van den Ende *et al*., 2004). Not only do plant fructans play a major role as storage carbohydrates, but they are also implicated in additional physiological functions in plants, such as drought and cold tolerance (Vijin and Smeekens 1999). By contrast, in bacteria, the multifunctional enzymes levansucrase (Meng and Fütter, 2003) and inulosucrase (van Hijum *et al*., 2003) catalyze fructan biosynthesis, producing inulin and levan, the predominant bacterial fructans, respectively. Details of the levan biosynthetic mechanism in bacteria

were recently revealed by structural studies of levansucrase (Meng and Fütter, 2003; Martinez-fleites *et al*., 2005).

Fructan-degrading enzymes that function primarily in the mobilization of stored fructans in plants and microbes have also been characterized. Just recently, the plant fructan hydrolases (EC 3.2.1) were found to catalyze the hydrolysis of levan and inulin *via* an exclusively exolytic mechanism, which releases successive terminal fructose units (Van Riet *et al*., 2006). The presence of these fructan exohydrolases, even in non-fructan-containing plants, suggests an additional, defensive role for these enzymes against pathogenic bacteria (Van den Ende *et al*., 2004).

In bacteria, two distinctly different classes of enzymes perform fructan degradation. One of these classes includes two hydrolases, levanase (EC 3.2.1.65) and inulinase (EC 3.2.1.7), which exhibit both endo- and exo-type hydrolytic activities. Classifications based on sequence similarity (Henrissat and Davies, 1997) (CAZy; www.cazy.org/CAZY/index.html) place these plant and microbial hydrolytic enzymes into the GH32 family (*O*-glycoside hydrolases). Structural analyses of the GH32 enzymes invertase (Alberto *et al*., 2004; Alberto *et al*., 2006), exo-inulinase (Nagem *et al*., 2004), and plant exohydrolase (Verhaest *et al*., 2005) have revealed substantial structural similarities; these enzymes consist of a five-bladed β-propeller domain

connected to a β-sandwich domain. In addition, active sites for the proposed hydrolytic activity have been identified; they include three acidic amino acid residues.

The second class of bacterial fructan-degrading enzymes, which includes levan fructotransferase (LFTase; EC 4.2.2.16) (Yang *et al*., 2002; Kim *et al*., 2005) and inulin fructotransferase (IFTase; EC 4.2.2.17 or 18) (Kang *et al*., 1998; Haraguchi *et al*., 2003), has long been known to catalyze the depolymerization of fructans into difructose dianhydrides (DFAs) *via* intramolecular fructosyl transfer (Fig. 1). Since DFAs have physiological effects, including the promotion of human health, and show promise as low-calorie sweeteners (reviewed in Ritsema and Smeekens, 2003), IFTase and LFTase have attracted the attention of the food industry. The linkage types of enzymatically produced DFAs vary with the specific enzymes and substrate fructans employed; IFTase produces DFA-I (α-$_D$-fructofuranose-β-$_D$-fructofuranose-2',1:2,1'-dianhydride) and DFA-III (α-$_D$-fructofuranose-β-$_D$-fructofuranose-2',1:2,3'-dianhydride), whereas LFTase results in DFA-IV (β-$_D$-fructofuranose-β-$_D$-fructofuranose-2,6':2',6-dianhydride) (Fig. 2). LFTases are categorized as GH32 enzymes, like other fructan hydrolases, and they share considerable sequence identity of 30 to 44% and several conserved regions with the other members of GH32 (Yang *et al*., 2002; Kim *et al*., 2005). In

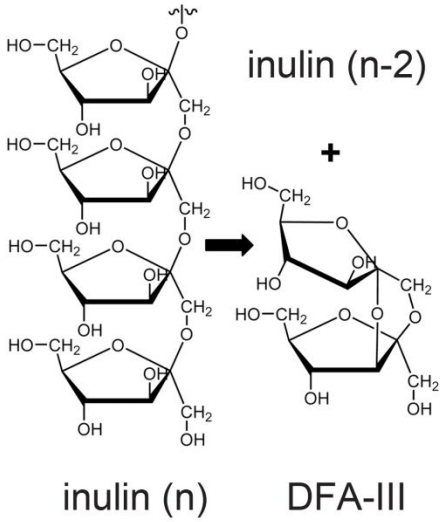

Figure 1. Schematic diagram of the substrate and product of the reaction by BsIFTase. Inulin is comprised of 30 to 50 units of fructosyl residues connected by a β-2,1 linkage to sucrose. Note that the product DFA-III has an inverted anomeric configuration at one fructosyl unit.

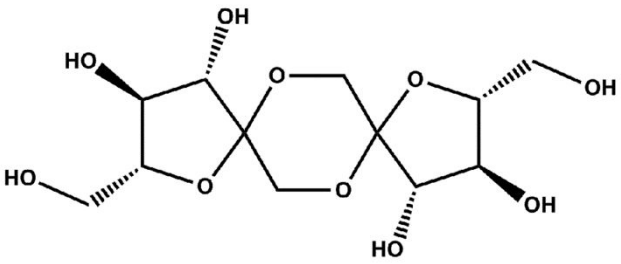

DFA I

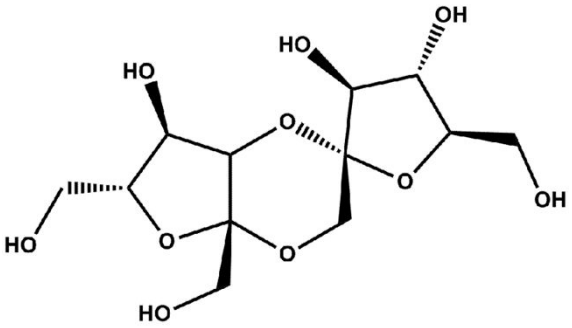

DFA III

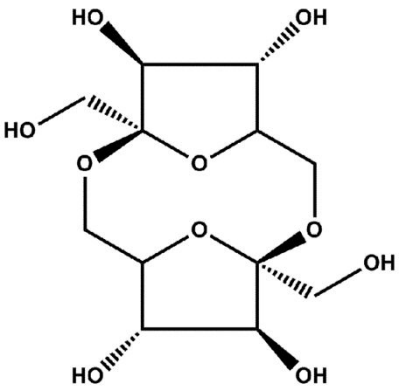

DFA IV

Figure 2. Structure of difructose anhydrides. DFA-I (α-$_D$-fructofuranose-β-$_D$-fructofuranose-2',1:2,1'-dianhydride); DFA-III (α-$_D$-fructofuranose-β-$_D$-fructofuranose-2',1:2,3'-dianhydride); DFA-IV (β-$_D$-fructofuranose-β-$_D$-fructofuranose-2,6':2',6-dianhydride).

recent years, the crystal structure of LFTase was reported as identical to those of other enzymes including to GH32 family, that consist of a five-bladed β-propeller N-domain and a β-sandwich C-domain (Park *et al*., 2012)

Notably, IFTases do not exhibit any apparent sequence homology with LFTases, although both enzymes carry out similar reactions. Furthermore, IFTases appear to be unrelated to any other known proteins, but are highly similar to members of the family, with 50 to 98% sequence identity (Fig. 3), suggesting that the IFTases share a three-dimensional structure common to the family. The products of six bacterial genes have so far been characterized biochemically as IFTases and classified as GH91 enzymes, even in the absence of supporting evidence for hydrolase activity. The DFA-I-producing IFTase characterized from *Arthrobacter globiformis S14-3* (EC 4.2.2.17) was cloned and expressed in *E. coli*, and the DFA-I as product was confirmed by enzyme reaction using ^{13}C NMR (Haraguchi *et al*., 1995). The DFA-III-producing IFTase from *Bacillus sp. snu-7* (BsIFTase; EC 4.2.2.18) consists of 450 amino acid residues, including a 40-residue, N-terminal signal sequence for secretion. Although biochemical features of BsIFTase have been characterized (Kang *et al*., 1998; Kim *et al*., 2007), the fundamental details of BsIFTase catalysis, such as the identities of the residues that catalyze intramolecular fructosyl transfer and the mode of enzyme action, remain elusive. To elucidate the

structural and functional properties of BsIFTase, its crystal structure at 1.8-Å resolution, and the structure of BsIFTase in a complex with a β-2,1-linked tetrafructosaccharide was determined. Together with the results of site-directed mutagenesis, those structural and functional analyses provide the first atomic resolution structures of IFTase and some details of its enzymatic mechanism.

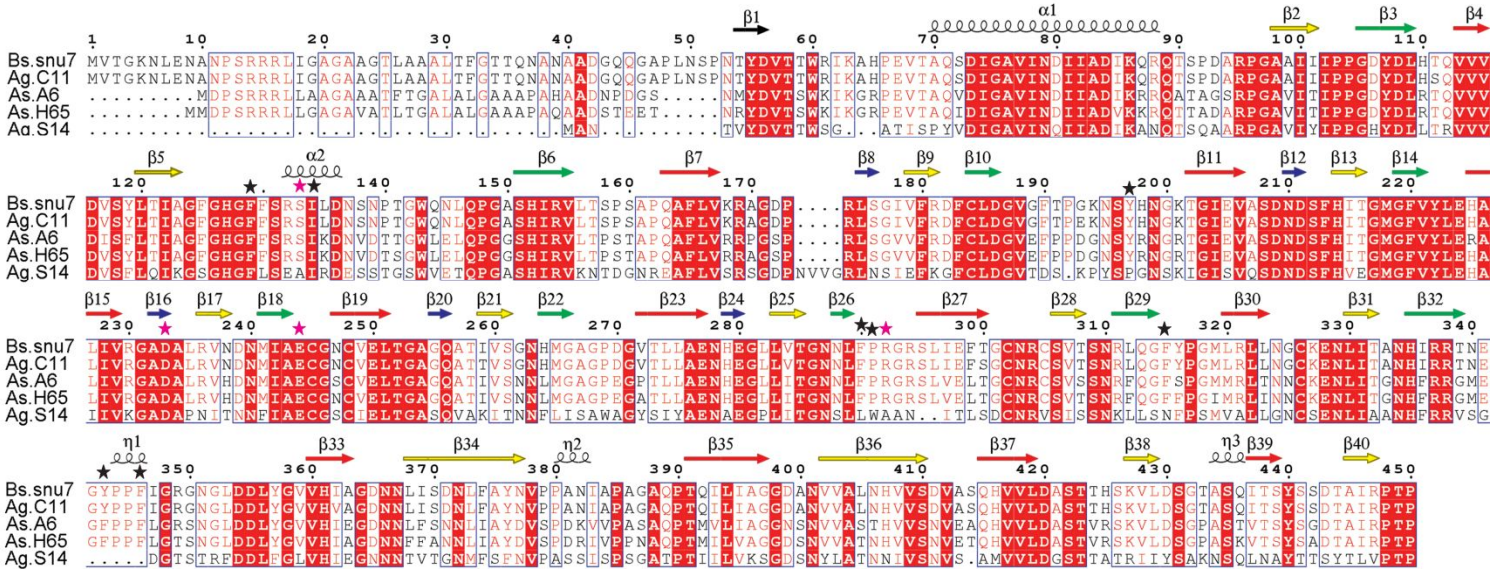
Bs.snu7
Ag.C11
As.A6
As.H65
Ag.S14

Figure 3. Sequence alignment of IFTase in various species. Multiple sequence alignment of IFTases from *Bacillus sp. snu-7* (Bs.snu7; GenBank accession #DQ112363), *Arthrobactor globiformis C11-1* (Ag.C11; AB009696), *Arthrobactor sp. A-6* (As.A6; AF124980), *Arthrobactor sp. H65-7* (As.H65; D84399), and *Arthrobactor globiformis S14-3* (Ag.S14; D38528). Note that the presented sequences are for precursors and sequence numbering is based on BsIFTase. Highly conserved residues are shown in red type and boxed in blue; strictly conserved residues are shown on a red background. Residues interacting directly with bound substrate are indicated with an asterisk in magenta, whereas other active site-forming residues are shown in black (see *Discussion* for details). The secondary structure elements are indicated by color-coding: red, PB1; blue, PB1b; yellow, PB2; green, PB3 (see text). Identical color codes for each β-strand are used throughout this publication. This figure was prepared using ESPript (Gouet *et al*., 1999).

MATERIALS AND METHODS

1. Purification and crystallization of BsIFTase

The gene for BsIFTase (access No. DQ112363) from the *Bacillus sp. snu-7* was cloned, and DNA for the mature BsIFTase (residues 41 to 450) was subcloned into the expression vector pET15b (Novagen, Madison, WI) using an *Nde*I and a *Sal*I site (Kim *et al*., 2007). The His-tagged, selenomethionine-substituted recombinant BsIFTase was prepared by transforming the expression plasmid construct into *E. coli* strain B834(DE3)*pLys*S, a methionine auxotroph (Novagen). The transformed cells were grown at 37°C and then induced for 4 h at 37°C with 1 mM IPTG and supplemented selenomethionine. Induced cells were harvested by centrifugation and sonicated in buffer A (50 mM NaH_2PO_4, pH 7.4, 500 mM NaCl). The His-tagged recombinant BsIFTase was purified using immobilized metal affinity chromatography with buffer B (buffer A + 500 mM imidazole), dialyzed against buffer C (50 mM Tris–HCl, pH 7.5, 200 mM NaCl, 1 mM EDTA), and then concentrated to ~10 mg/ml.

Crystallization was accomplished at 22°C using the hanging-drop vapor-diffusion method. Crystals of BsIFTase in space group *C2* with three monomers per asymmetric unit were produced using the His-tagged,

selenomethionine-substituted protein with a crystallization buffer consisting of 0.1 M imidazole, pH 8.0, 0.2 M NaCl, and 1.0 M $(NH_4)_2HPO_4$ (Fig. 4). The BsIFTase–tetrafructosaccharide complex was obtained by soaking the BsIFTase crystals for 90 min in a crystallization solution containing 200 mM substrate (see below). The crystal parameters are shown in Table 1. Crystallization of IFTase from *Arthrobacter globiformis* has been described previously, but the structure has not been reported (Momma *et al*., 2003).

2. Purification of tetrafructosaccharides

Tetrafructosaccharides, which serve as the minimal substrate for BsIFTase activity (Kim *et al*., 2007), were initially produced by an enzymatic reaction between inulin and purified endoinulinase from *Arthrobacter sp. S37* (Kim *et al*., 2005); this enzyme produces oligosaccharides by endolytic degradation of inulin. The reaction products were subjected to charcoal-celite column chromatography, and the tetrafructosaccharides were eluted stepwise with 7% ethanol. Purified tetrafructosaccharides were freeze-dried for storage, and their chemical composition and purity were verified using thin-layer chromatography (see below).

3. Data collection and structure determination

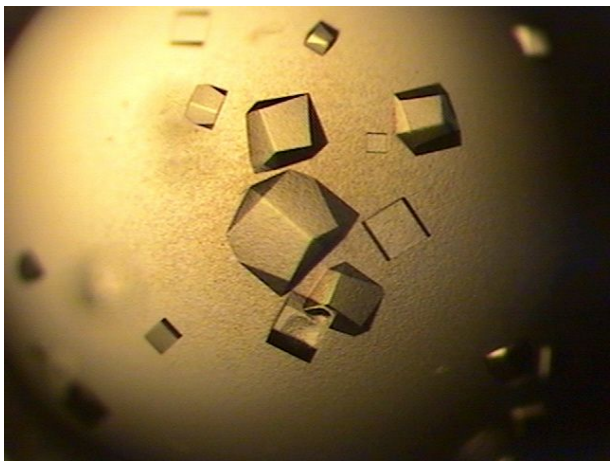

Figure 4. Crystals of His-tagged IFTase. IFTase crystals were performed in a various crystallization condition. IFTase crystals to collect diffraction data were obtained in buffer composed of 0.1 M imidazole, pH 8.0, 0.2 M NaCl, and 1.0 M $(NH_4)_2HPO_4$.

Multiwavelength anomalous dispersion (MAD) data for crystals of selenomethionine-substituted BsIFTase were collected at 1.8 Å on beamline 6B at Pohang Accelerator Laboratory, Pohang, Korea. Diffraction data for the BsIFTase–tetrafructosaccharide complex at 1.8 Å resolution were collected using a single wavelength on beamline 6B at Pohang Accelerator Laboratory (Fig. 5). Data were collected at 100 K, and the crystals were cryoprotected by addition of 30% glycerol to each crystallization solution. The program HKL2000 was used for data processing (Otwinowski and Minor, 1997).

The program SOLVE/RESOLVE (Terwilliger and Berendzen, 1999; Terwilliger, 2000) was used for phasing and density modification of the native BsIFTase structure. Of 12 possible selenium atoms, a total of 10 sites were identified and used to calculate the initial phases. The presence of three monomers in the asymmetric unit improved density modification in RESOLVE with non-crystallographic symmetry (NCS) averaging. The initial electron density map was sufficient to trace most of the residues in each monomer, except the highly disordered N-terminal region including the His-tag and residues 41 to 51. Manual model building and refinement were performed using the programs O (Jones *et al*., 1991) and CNS (Brunger *et al*., 1998), respectively.

The substrate-binding site was unambiguously located using a

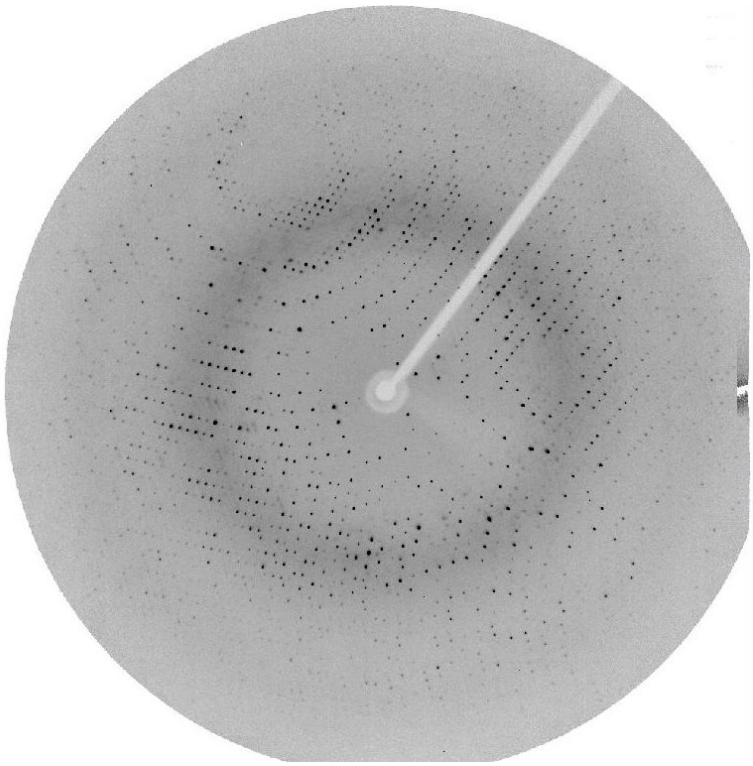

Figure 5. Diffraction of His-tagged IFTase crystal. Diffraction data of His-tagged IFTase crystals were collected at 1.8 Å resolution on beamline 6B at Pohang Accelerator Laboratory, Pohang, Korea. The crystals belonged to the monoclinic space group *C2*.

difference map with phases from the substrate-free native enzyme and amplitudes between the substrate-bound and native data. The difference map showed that only a disaccharide moiety of the tetrasaccharide was observed and a conformation of the identified difructosaccharide corresponds to that of substrate, not the product DFA-III. Presumably, high concentration of substrate (200mM) led to stabilization of substrate binding in the active site. A model for the bound difructosaccharide was subsequently fit into the density, and the resulting model for the BsIFTase–substrate complex was then subjected to refinement using CNS. The residual density near the binding site could not be explained by any molecular model and was therefore modeled as water molecules (W106, W118, W159). Two molecules of phosphate were modeled in the putative intersubunit channel. Details of data collection and structure refinement are shown in Table 1. The stereochemistry of refined structures was confirmed using the program PROCHECK (Collaborative Computational Project Number 4, 1994). With the exception of one residue Val188 in each monomer, neither the native nor substrate-bound structures contained residues with disallowed conformations. The figures were prepared using PyMOL (DeLano, W.L. The PyMOL Molecular Graphics System), and the structure was analyzed using CCP4 suite (Collaborative Computational Project Number 4, 1994).

Table 1. Data collection, phasing and refinement statistics for MAD (SeMet) structures.

	IFTase-SeMet			IFTase-substrate
Data collection				
Space group	C2			C2
Cell dimensions				
a, *b*, *c* (Å)	159.1, 91.9, 93.0			159.1, 92.0, 92.9
α, β, γ (°)	90, 124.8, 90			90, 124.8, 90
	Peak	*Inflection*	*Remote*	
Wavelength	0.97912	0.97923	0.97144	1.12714
Resolution (Å)	30.0-1.8 (1.86-1.8)[a]	30.0-1.8 (1.86-1.8)	30.0-1.8 (1.86-1.8)	50.0-1.8 (1.86-1.8)
R_{sym} or R_{merge}[b]	10.5 (48.3)	10.3 (51.5)	10.2 (55.3)	7.0 (28.6)
$I / \sigma I$	19.8 (2.9)	20.0 (2.9)	19.8 (2.8)	29.6 (5.0)
Completeness (%)	100 (99.9)	100 (100)	100 (99.9)	100 (100)
Redundancy	7.4 (7.2)	7.4 (7.2)	7.4 (7.1)	7.0 (6.9)
Refinement				
Resolution (Å)	30.0-1.8			50.0-1.8
No. reflections	75,480 / 8,377			83,721 / 9,334
R_{work}[c] / R_{free}	19.8 / 22.6			20.7 / 22.7
No. atoms				
Protein	8,946			8.946
Ligand/ion	8			77
Water	576			625
Average *B*-factors (Å^2)				
Protein	14.3			15.7
Ligand/ion	57.6			33.9
Water	25.4			24.4
R.m.s deviations				
Bond lengths (Å)	0.011			0.012
Bond angles (°)	2.41			2.43
Ramachandran plot				
Favored (%)	85.5			85.4
Allowed (%)	14.2			14.3

Single crystals were used for each data set.
[a]Numbers in parentheses refer to data in the highest resolution shell.
[b]$R_{merge} = \Sigma|I_h - \langle I_h \rangle| / \Sigma I_h$, where I_h is the observed intensity and $\langle I_h \rangle$ is the average intensity.
[c]$R_{work} = \Sigma ||F_{obs}|-k|F_{cal}|| / \Sigma|F_{obs}|$, [d]$R_{free}$ is the same as R_{obs} for a selected subset (10%) of the reflections that was not included in prior refinement calculations.

4. Site-directed mutagenesis and enzymatic activity assay

Genes encoding BsIFTase mutants were generated from plasmid pET15b-BsIFTase using the polymerase chain reaction (Table 2), and their sequences were verified by DNA sequencing. The mutant proteins were expressed and purified as His-tagged recombinant proteins in *E. coli* strain BL21(DE3)*pLys*S as described above, and each of the purified proteins appeared as a single major band on SDS–PAGE. BsIFTase enzyme activity was assayed as reported previously (Kang *et al*., 1998; Kim *et al*., 2007), using 1 μg of wild-type or mutant BsIFTase in a 100-μl reaction mixture containing 0.5% inulin in 50 mM Tris-HCl (pH 7.5). The reaction mixtures were incubated at 37°C for 5 min and then their products were analyzed by thin-layer chromatography in a solvent system of *n*-propanol:ethylacetate:H_2O (3:1:1).

5. Analytical ultracentrifugation

Equilibrium sedimentation studies were performed using a Beckman ProteomeLab XL-A analytical ultracentrifuge using six-hole, charcoal-filled Epon centerpieces. BsIFTase was dissolved at 1.8 μM (0.08 mg/ml), 3.6 μM (0.16 mg/ml), or 7.2 μM (0.32 mg/ml) in a buffer containing 50 mM Tris-HCl, pH 7.5, 0.2 M NaCl, and 1 mM EDTA. The concentration of the protein was

Table 2. Primer sequences of mutants.

D233N	
Forward	5’-CGTGCGCGGCGCGAACGCACTCCGCGTCAACG-3’
Reverse	5’-GTTGACGCGGAGTGCGTTCGCGCCGCGCACG-3’
E244Q	
Forward	5’-GACAACATGATCGCCCAATGTGGCAACTGCGTC-3’
Reverse	5’-GACGCAGTTGCCACATTGGGCGATCATGTTGTCG-3’

determined using ε_{280nm} = 27,765 $M^{-1}cm^{-1}$ calculated from its amino acid composition. The radial absorbance distribution was measured at 20°C and 12,000 rpm at four different wavelengths (230, 235, 240, and 280 nm). After 48 h of centrifugation, five scans were collected and averaged for the analysis. A partial specific volume of 0.7265 cm^3/g and a buffer density of 1.00808 g/cm^3 at 20°C were calculated using Sednterp (Laue *et al*., 1992). For data analysis by mathematical modeling using non-linear least-squares curve-fitting, the fitting function was $C_r = C_b \exp(A_p M_p(r^2-r_b^2)) + \varepsilon$, where $A_P = (1-v\rho)\omega^2/2RT$, C_r is the total concentration at the radial position r, C_b is the concentration of protein at the bottom of the cell, M_p is the molecular weight of protein, v is the partial specific volume, ρ is the solution density, ω is the angular velocity of the rotor, and ε is a baseline error term. The data were analyzed by mathematical modeling using MLAB (Knott, 1979). All measured data fit well to a trimeric model, and a representative result obtained for 1.8 μM BsIFTase is presented.

6. Isothermal titration calorimetry

Isothermal titration calorimetric analysis was carried out using MicroCalorimetry System (Microcal) at 25°C. Two inactive mutants E244Q and D233N, as well as substrate inulin were dialyzed against a buffer

containing 50 mM Tris–HCl, pH 7.5, 200 mM NaCl, 1 mM EDTA, and then degassed. Data were analyzed using the Origin software (OriginLab Corp.).

RESULTS

1. Overall structure of monomer

Mature BsIFTase consisting of amino acid residues 41 to 450 was crystallized in the *C2* space group with three monomers (A, B, and C) per asymmetric unit related by NCS. The presence of a homotrimeric BsIFTase in a crystalline state is consistent with results obtained from analytical ultracentrifugation experiments (Fig. 6), which indicate that the enzyme exists exclusively as a trimer *in solution* at concentrations as low as 0.08 mg/ml. In size-exclusion chromatography, however, BsIFTase appeared to behave as a dimer, possibly because of its elongated shape (Fig. 7).

Each monomer forms a right-handed parallel β-helix (henceforth, "β-helix"), a fold that was initially identified in the pectate lyase, PelC (Yoder *et al*., 1993). Beta-helical folds have been identified in several classes of enzymes frequently associated with polysaccharides, including pectin lyase-related proteins (Herron *et al*., 2000), pectin methylesterase (Matteo *et al*., 2005), and phage P22 tailspike protein (TSP) (Steinbacher *et al*., 1996). Recently, they have also been found in other polysaccharide-degrading enzymes in GH families 28 (van Santen *et al*., 1999), 49 (Larsson *et al*., 2003), and 82 (Michel *et al*., 2003), as well as in virulence factors (Jenkins and

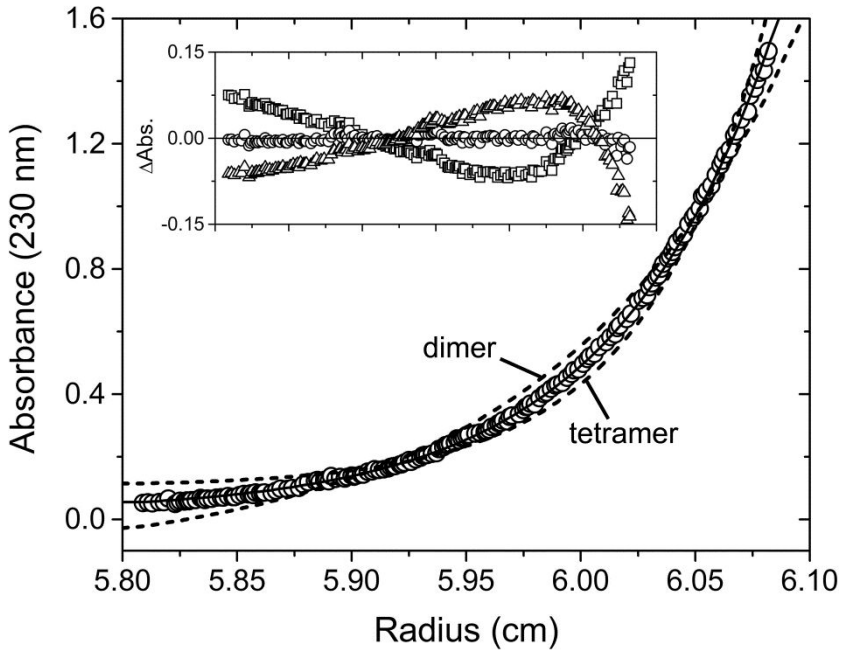
Absorbance (230 nm)
Radius (cm)
1.6
1.2
0.8
0.4
0.0
5.80
5.85
5.90
5.95
6.00
6.05
6.10
dimer
tetramer
ΔAbs.
0.15
0.00
-0.15

Figure 6. Oligomerization state of BsIFTase using analytical ultracentrifugation. Typical equilibrium sedimentation data obtained at 230 nm and 12,000 rpm with 1.8 μM (0.08 mg/ml) BsIFTase were fit to dimer, trimer, and tetramer models. The absorbance distribution is consistent with a thermodynamically ideal trimer (solid line), not with a dimer or tetramer (dashed line). (*Insert*) The distributions of the residuals as a function of radial position indicate that the trimer model (open circles) yielded the smallest root-mean-square error of 7.54×10^{-3}, whereas the dimer and tetramer models deviated significantly from the measured data (rectangles and triangles, respectively). This result was obtained from experiment executed by prof. Kim, S. J. in Mokpo National University.

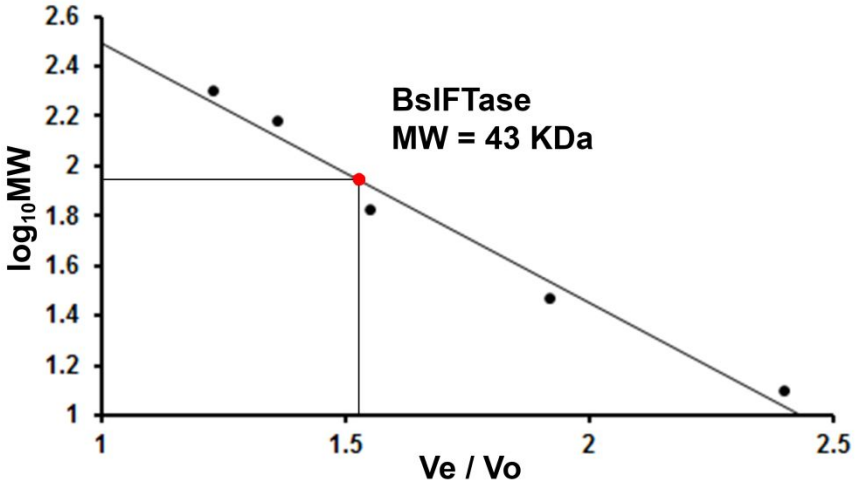

	Molecular Weight (MW)	Ve / Vo	$\log_{10}$ MW
β-Amylase	200	1.23	2.30
Alcohol dehydrogenase	150	1.36	2.17
Bovine serum albumin	66	1.55	1.82
Carbonic anhydrase	29	1.92	1.46
Cytochrome C	12.4	2.40	1.09
BsIFTase	43*	1.53	1.94 (87KDa)

Figure 7. Oligomerization state of BsIFTase using size exclusion chromatography. The molecular characteristic of BsIFTase in solution state was measured using analytical size exclusion chromatography. The elution volumes (Ve) of five standard samples are divided by the void volume (Vo) that is determined by Blue dextran of 2000 KDa molecular weight, and plotted against the logarithm of the MW of the standard samples. The approximate molecular weight of BsIFTase was calculated 87KDa from the standard curve, which appears to act as a dimer in solution state. In this table, the molecular weight of BsIFTase marked with asterisk was calculated using protein molecular weight prediction program based on protein sequence.

Pickersgill, 2001). The BsIFTase monomer, which is shown in Fig. 8A, has dimensions of 75 × 57 × 30 Å. Each monomer has an overall cylindrical shape consisting of 399 residues that form 13 helical turns of a right-handed coil. The highly disordered *N*-terminal residues 41 to 51 are excluded from the final model. The BsIFTase structure exhibits the general structural characteristics of β-helical proteins (Jenkins and Pickersgill, 2001; Jurnak *et al*., 1994; Jurnak and Yoder, 1995), but it differs in some details. Each turn consists of two, three, or four β-strands, joined by intervening loops, and the β-strands that are present between adjacent turns associate to form a parallel sheet on the surface of the enzyme. All of the β-strand residues fulfill two strict structural requirements: they are in the β-conformation region of a Ramachandran plot, and the main-chain atoms of β-strands in adjacent turns interact by hydrogen bonding (Fig. 9). A structure-based sequence alignment of the β-strands along the β-sheet is shown in Fig. 8B. Of particular interest is the fact that the N-terminal five turns (turns 3–7) of the coil involve four β-strands, whereas turns 8 and 9 include three, and the C-terminal four turns involve only two β-strands each (Fig. 8A, B). Each β-strand consists of two to six residues, except that the β-strands in turns 10 and 11 have 10 and 9 residues, respectively. As a consequence of variation in the number of β-strands and loop length, the N-terminal turns exhibit wider interiors, with a 19-residue α1-helix capping the

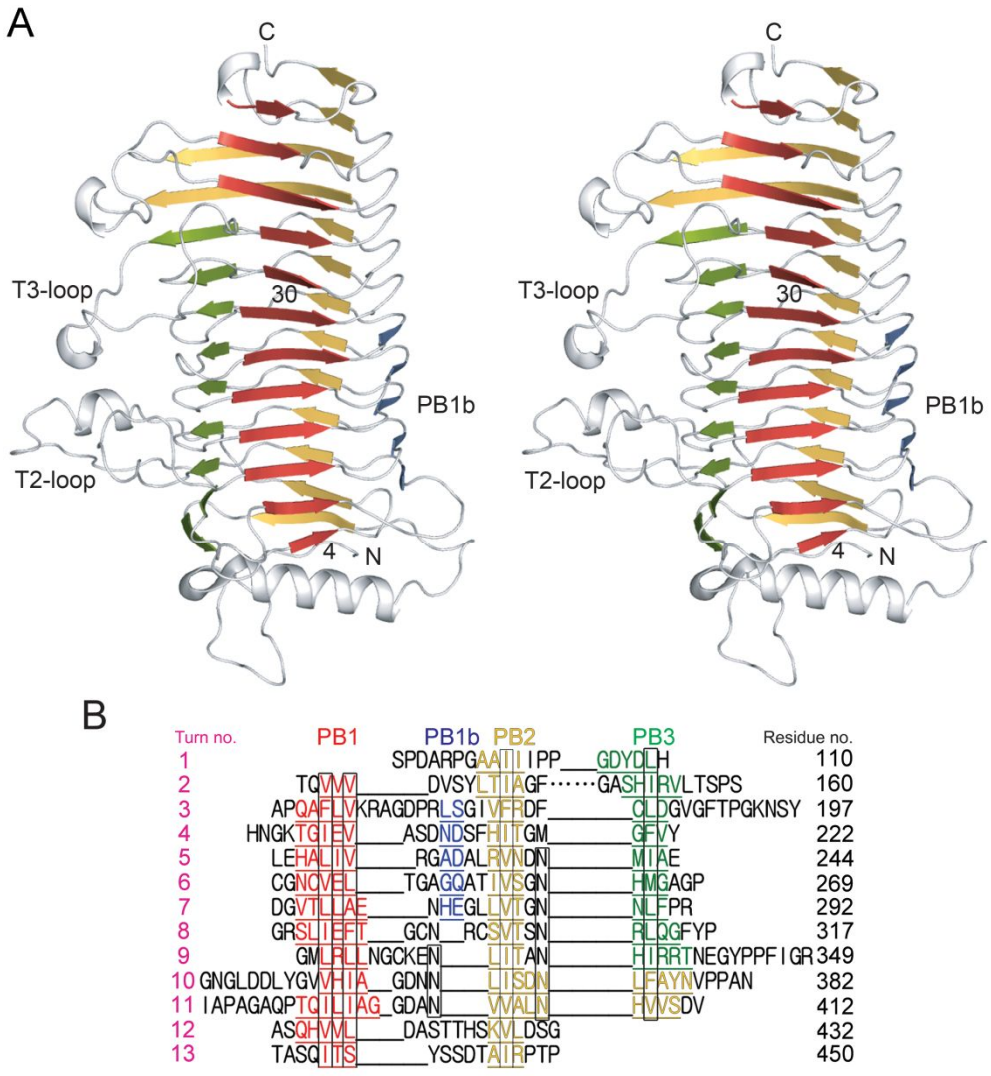
A
C
T3-loop
30
PB1b
T2-loop
4
N
C
T3-loop
30
PB1b
T2-loop
4
N
B
Turn no.
PB1
PB1b
PB2
PB3
Residue no.
1 SPDARPGAATII IPP GDYDLH 110
2 TQVMV DVSYLTTAGF GASHIRVLTSPS 160
3 APQAFLVKRAGDPRLSGIVFRDF CLDGVGFTPGKNSY 197
4 HNGKTGIEV ASDNDSFHITGM GFVY 222
5 LEHALTV RGADALRVNDN MIAE 244
6 CGNCVEL TGAGQATIVSGN HMGAGP 269
7 DGVTLLAE NHEGLLVTGN NLFPR 292
8 GRSLIEFT GCN RCSVTSN RLQGFYP 317
9 GMLRLL NGCKEN LITTAN HIRRTNEGYPPFIGR 349
10 GNGLDDLYGVVHIA GDNN LITSDN LFAYNVPPAN 382
11 IAPAGAQPTQILIAG GDAN VVALN HVVSDV 412
12 ASQHVVL DASTTHSKVLDSG 432
13 TASQITS YSSDTAIRPTP 450

Figure 8. Overall structure of BsIFTase. (A) Side view of monomeric BsIFTase is shown in stereo, with PB1 labels for turns 2 and 9. Two active site-forming loops are indicated (see text). Each β-strand is defined in Fig. 1B. (B) Structure-based sequence alignment for equivalent β-strands, with corresponding turns labeled. The color-coding for each β-strand is identical to that used in Fig. 1A, and stacked side chains are enclosed in a black box. For clarity, residues 126 to 148 in T2 of turn 2 are indicated only by a dashed line.

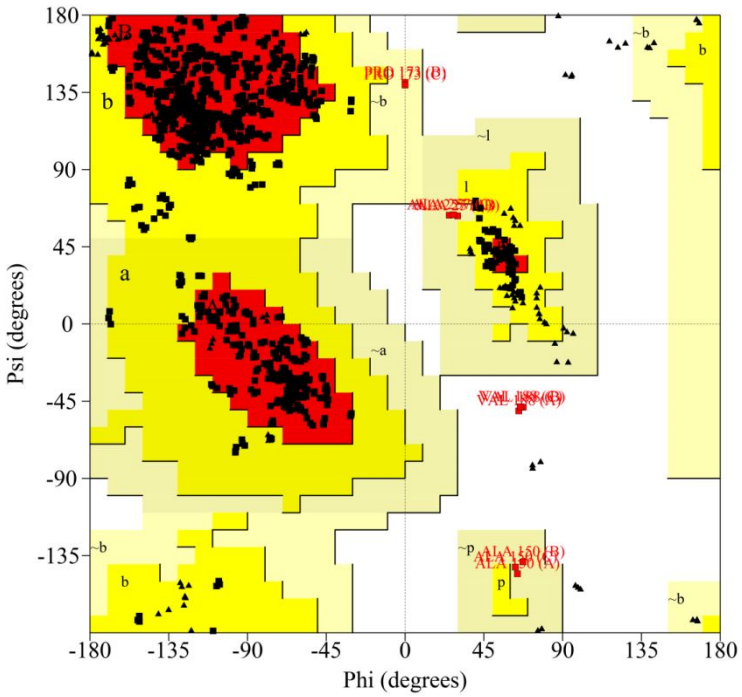

Figure 9. The Ramachandran plot of BsIFTase structure. One residue Val188 in each monomer contained to disallowed conformations. Glycine residues are separately distinguished by triangles, which are not restricted to the regions of the plot for the other amino-acid side chains.

N-terminal domain, whereas the last two turns at the C-terminus have narrow interiors with only two β-strands.

2. Structural characteristics of turns

The BsIFTase turns are partially homologous to three-β-strand turns of PelC (Yoder *et al*., 1993; Jurnak *et al*., 1994; Jurnak and Yoder, 1995). In PelC, the first, second, and third β-strands of the turns are designated PB1, PB2, and PB3, respectively, with loops T1, T2, and T3 following the corresponding strands (Fig. 10B). In BsIFTase, an additional two-residue β-strand is present within the four-β-strand turn at the region corresponding to T1 of PelC; this strand is designated PB1b (Fig. 10A). The second strand in the two-β-strand turns is designated PB2 because its location is equivalent to that of PB2 in a three-β-strand turn (see below). The long β-strands in turns 10 and 11 include all three regions (PB2, T2, and PB3; Fig. 8B and 10C). In cross-section, the turns resemble an "L" shape, with the β-strands almost perpendicular to each other. The most dramatic changes in β-strand conformation were observed at turns 10 and 11, in which the 10- and 9-residue PB2 strands are so sharply bent that the two PB2 ends are almost perpendicular. As a result, the first half of PB2 in these turns corresponds structurally to PB2, but the second half of PB2 is equivalent to PB3 in other turns (Fig. 10B and C).

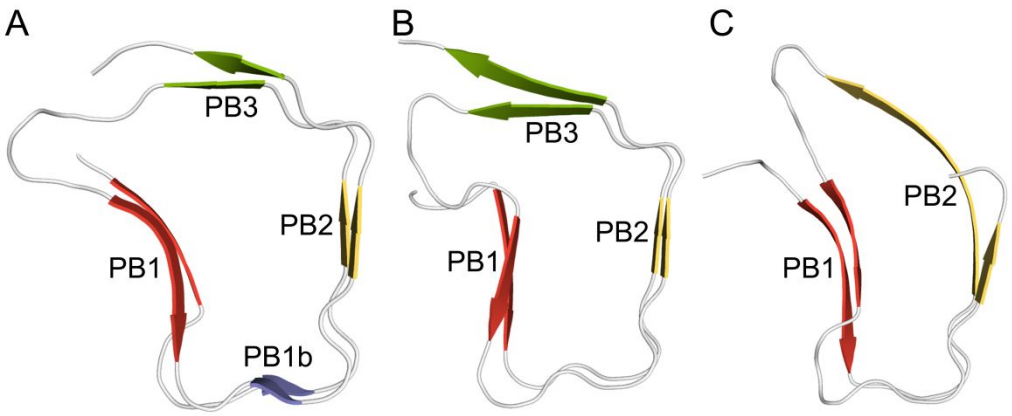

Figure 10. Structural conformation of the BsIFTase turns. (A) Turn 3 to 7 is composed of four-β-strands, PB1, PB1b, PB2, and PB3 which are almost perpendicular to each other. (B) Turn 8 and 9 are three-β-strand turns similar to PelC. (C) The long β-strands in turns 10 and 11 are represented in company with the short β-strands in turn 12 and 13.

Although the BsIFTase structure differs from that of most other β-helical proteins in the number and conformation of β-strands in turns, it does resemble these proteins in that the interior of the β-helix is closely packed with hydrophobic or polar side chains along the sheet (Jenkins and Pickersgill, 2001; Jurnak *et al*., 1994; Jurnak and Yoder, 1995). Specifically, the internal hydrophobic resides, which include valine, leucine, and isoleucine predominantly, and occasionally phenylalanine, are stacked between adjacent turns, as indicated in the structure-based sequence alignment of the β-strands shown in Fig. 8B. PB1 has two rows of hydrophobic stacks, and PB2 and PB3 have one stack each, with each stack involving a total of 11 to 13 residues (Fig. 11A).

With the exception of the 27-residue T2 loop in turn 2, the T2 loops are only two or three residues in length. Sharp kinks in a T2 loop are associated with a stack of seven asparagine residues that is located in the β-helix interior (Fig. 8B); this was first identified in the structure of PelC and is called the "asparagine ladder" (Yoder *et al*., 1993). In BsIFTase, this asparagine ladder, including Asn372 in turn 10 and Asn406 in turn 11, has a continuous hydrogen-bonded network between the asparagine side chains and forms hydrogen bonds between the main-chain amide groups in a T2 loop of adjacent turns and the asparagine side chain (Fig. 11B); consequently, the

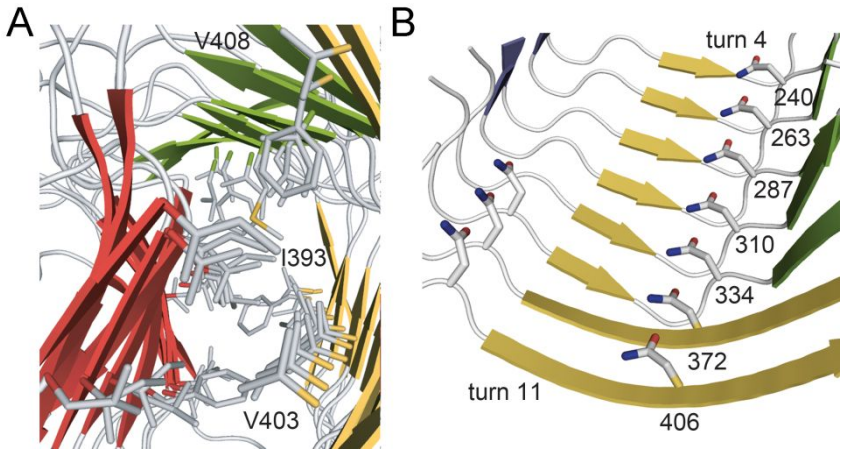

Figure 11. Internal structure of monomeric BsIFTase. (A) The stacked internal, hydrophobic side chains are presented in a top view from the C-terminus, with labeled residues. (B) Stacked asparagine residues in T1 and T2 are shown with their turn and residue numbers.

ladder stabilizes the sharp kinks.

Unlike T2 loops, T3 loops following PB3 strands exhibit a wide range of lengths and conformations. The T3 loops in turns 3, 9, and 10 protrude from the core β-helix, forming a relatively irregular protrusion on one side of the enzyme. In the central portion of the β-helix, the β-helix surface consists primarily of T3 loops. Notably, the protruding 27-residue T2 loop in turn 2 also wraps halfway around the β-helix and is localized in this loop cluster (Fig. 8A).

3. Trimeric structure of BsIFTase

The three parallel monomers in the asymmetric unit intertwine to constitute a trimer (Fig. 12) in which PB2 in one monomer is packed in an anti-parallel manner against PB3 in the adjacent monomer. When the three monomers are superimposed, the resulting rmsd for the corresponding Cα atoms is 0.05 Å, indicating that the structures of the independent monomers are essentially identical.

In contrast to the interior side chains, the external side chains of each BsIFTase sheet are relatively heterogeneous in amino acid composition and configuration. The side chains of adjacent subunits interdigitate, which stabilize the trimer (Kreisberg *et al*., 2002; Simkovsky and King, 2006). The

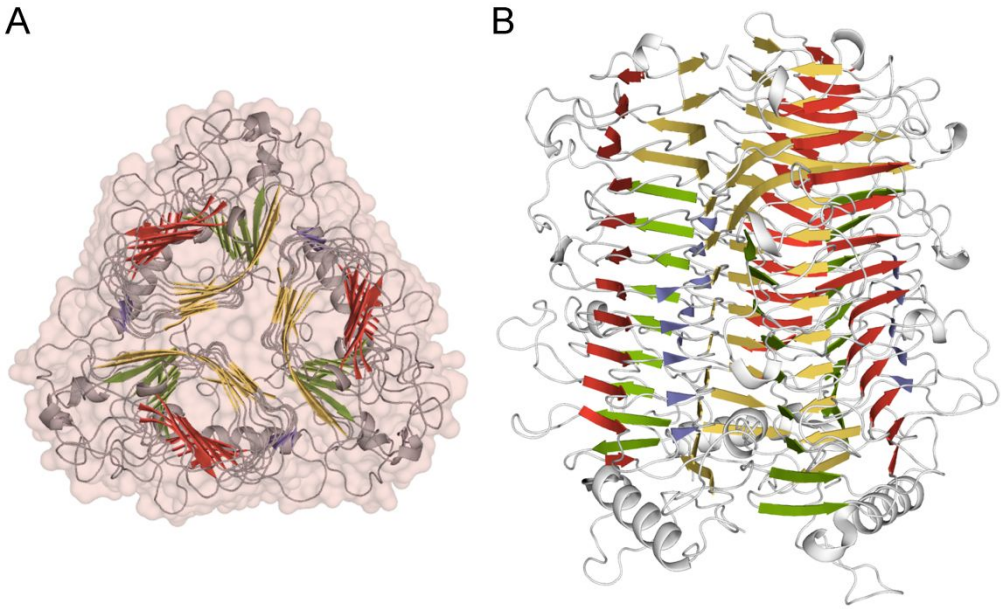

Figure 12. The overall structure of BsIFTase trimer. (A) Top view of a BsIFTase trimer in an asymmetric unit is overlaid with surface model. The helical axis is perpendicular to the plane of the figure. The would-be intersubunit channel parallel to the helical axis is located at the center of the trimer but is closed. (B) Side view of a BsIFTase trimer is shown as cartoon representation.

surface area buried by trimerization is calculated to be 4439 $Å^2$ per monomer, or 28% of the monomer surface area. Due to this close packing, no inter-subunit channel is present between monomers or at the trimer interface. Specifically, in the channel that otherwise might be present in the center of the trimer, the only electron density observed arose from several water molecules and from two phosphate molecules from the crystallization buffer.

4. Substrate binding site at the monomer-monomer interface

The structure of BsIFTase complexed with a β-2,1-linked tetrafructosaccharide revealed that the substrate is bound in the crevice between two interacting monomers. Therefore, three NCS-related, independent, but structurally identical, binding sites are present in the trimeric complex (Fig. 13A). Only a disaccharide moiety of the tetrasaccharide was unambiguously observed (Fig. 13B). Although inulin is a non-reducing fructan, the BsIFTase region interacting with the terminal fructosyl residue was assigned as subsite +2 following the nomenclature of Davies (Davies *et al.*, 1997). The terminal fructose F1 (subsite +2) is linked to another fructose F2 (subsite +1) by a β-2,1 glycosidic bond. Weak residual density corresponding to another glycosidic bond to F3 (subsite −1) was observed, but the density was so disordered that the third fructose unit was not included in the final model.

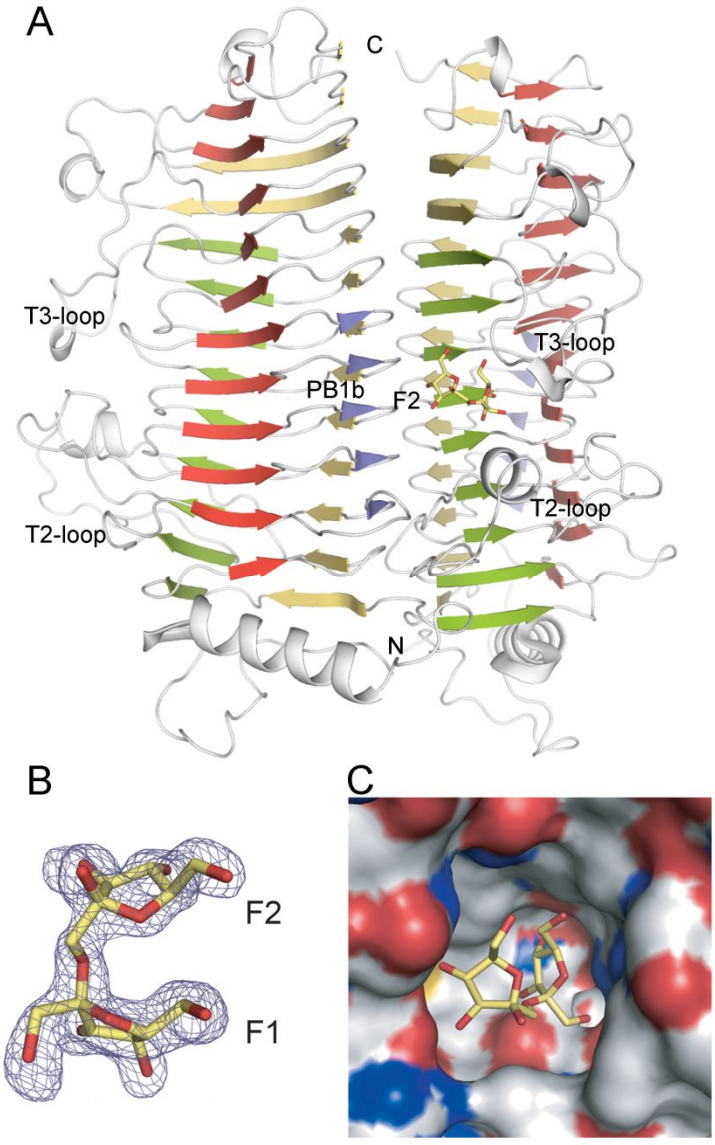
A
C
T3-loop
T3-loop
PB1b
F2
T2-loop
T2-loop
N
B
F2
F1
C

Figure 13. The active site in a BsIFTase trimer. (A) Side view of a BsIFTase trimer with F2 reveals the active site located in an interface between two monomers. (B) The final $2F_o–F_c$ electron density map contoured at 1.0 σ is overlaid on the model for difructosaccharide, with labels of F1 and F2 (see text). (C) The molecular surface for the substrate binding site is shown with a bound disaccharide represented by a stick model. Negative and positive electrostatic potentials are indicated in red and blue, respectively.

The structure of the BsIFTase substrate-binding pocket occupied by the observed disaccharide F1–F2 is shown in Fig. 13C and 14A, and the interactions between BsIFTase and the bound substrate are shown schematically in Fig. 14B. In particular, the substrate binding site is located on the surface between (*i*) the regions including PB3 and T3 of turns 5 to 7 and (*ii*) PB1b of turns 4 to 6 from the interacting subunit. Two additional structural elements— loop T3 from turn 9 and loop T2 from turn 2—enclose the top and bottom of the substrate binding site, respectively, generating a pocket between two interacting monomers. The pocket is wide open at the entrance, which is comprised of PB1b and loop T3 from turn 9, and terminated by a layer of polar residues, including Ser133, Arg292, and Glu244. This 10-Å-deep pocket is lined by hydrophobic residues, including Phe129, Ile134, Tyr197, Phe290, Pro291, Phe315, Tyr343, and Phe346, as well as polar residues Arg174* and Asp233* from the neighboring monomer. All active site residues are either invariant or highly conserved within the family (Fig. 3).

Substrate binding appears to cause insignificant, but systematic, localized structural changes in the loop region including Tyr343 (see Fig. 14A). Loop T3 residues Glu341 to Arg349 in the pocket are shifted toward the substrate, with the Cα atoms moving 0.4 to 1.0 Å for an overall Cα rmsd of 0.16 Å. Except for these variations, no other conformational differences, even

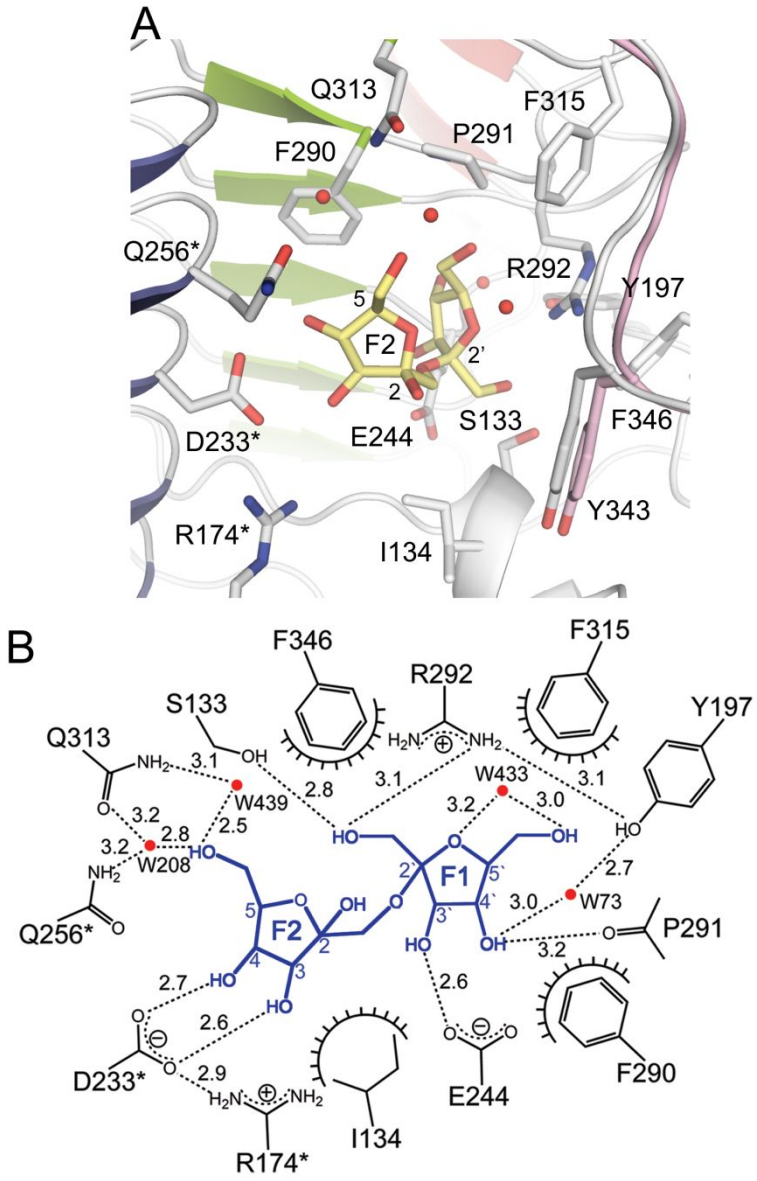
A
Q313
F315
P291
F290
Q256*
R292
Y197
F2
D233*
E244
S133
F346
Y343
R174*
I134
B
F346
F315
R292
S133
Y197
Q313
W433
W439
W208
F1
F2
W73
P291
Q256*
F290
D233*
E244
I134
R174*

Figure 14. A close-up view of the active site in the substrate-binding form. (A) The BsIFTase active site is shown, including the amino acid residues and water molecules (red circle) interacting with the bound disaccharide. Residues from an adjacent subunit are indicated by an asterisk. The orientation is identical to that of Figure 9 (C). Note that a region including a loop T3 in the native structure is indicated in light-pink, with an indication of Tyr343. This loop shows a localized conformation change by the binding of a substrate. See text for details. (B) Schematic diagram of the interaction between a bound disaccharide and residues in the BsIFTase active site. The dashed lines indicate putative hydrogen bonds, which are labeled with the averaged interatomic distance (Å) in three active sites, and the decorated arcs represent van der Waals interactions of less than 5.0 Å for a disaccharide bound in the active site.

in side-chain configuration, were observed between the native structure and the substrate complex. An apparent feature of the bound F1−F2 is the relative orientation of the two fructose units; a furanose ring of F2 is not stacked with but, rather, is oriented perpendicular to F1. This conformation is similar to that previously determined for DFA-III (Taniguchi and Uchiyama, 1982).

Only six direct interactions between the bound disaccharide and active site residues are observed in the crystal structure (Fig. 14B). Four of these interactions are localized in F1 bound at the inner site; the hydroxyl group O-1' (primed numbers refer to F1 atoms) interacts with the side chains of Arg292 and Ser133 at distances of 3.1 and 2.8 Å, respectively, and the O-3' hydroxyl group is 2.6 Å from the carboxylate group of Glu244. The main-chain carbonyl group of Pro291 also hydrogen bonds with O-4'. Fructose F2, which is close to the entrance of the active site, hydrogen bonds with Asp233* from a neighboring monomer; Asp233* mediates bidentate hydrogen bonds with O-3 and O-4 of F2 at distances of 2.6 and 2.7 Å, respectively. A potential 2.9-Å hydrogen bond with the guanidinium group of Arg174* may further stabilize the orientation of Asp233*. Solvent-mediated hydrogen bonds are found at O-6 of F2 and O-4' of F1. Of these substrate-interacting residues, Arg174, Asp233, and Glu244 are invariant in the IFTase family (Fig. 3), suggesting that they have important roles in catalysis or substrate binding. The

interactions described here were consistently observed at each of the three independent binding sites of the BsIFTase trimer.

5. Site-directed mutagenesis of BsIFTase

The functional roles of residues Asp233 and Glu244, which interact directly with the bound disaccharide, were examined using site-directed mutagenesis. The enzymatic activities of the resulting mutant proteins were measured using thin-layer chromatography (Fig. 15). Wild-type BsIFTase predominantly produced DFA-III, as well as by-products such as GF3 and GF4, whereas mutants D233N and E244Q were essentially inactive.

6. Binding of substrate to the mutant BsIFTase

Since two mutants D233N and E244Q were inactive, it was possible to measure the binding affinity of substrate inulin to these mutants by isothermal titration calorimetric analysis (Fig. 16). Substrate inulin readily binds both mutants, with its K_d of 23.1μM and 68.5μM for D233N and E244Q, respectively.

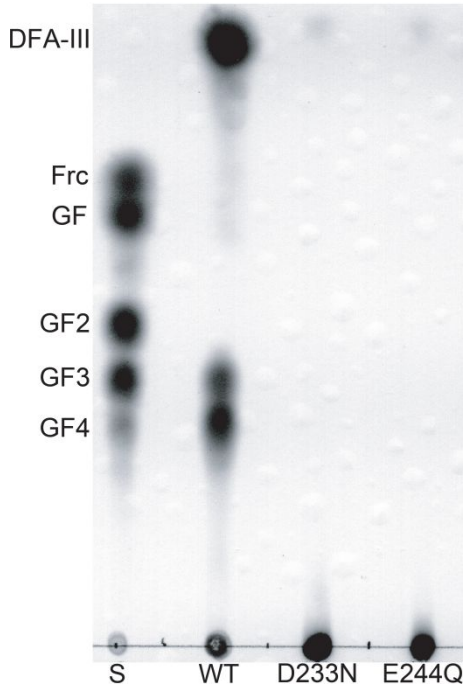

Figure 15. Thin-layer chromatogram of the reaction products of wild-type and mutant BsIFTases. Lane S depicts a standard mixture of carbohydrates including fructose monomer (Frc) and GF, GF2, GF3, and GF4, in which a mono-, di-, tri- or tetrafructosaccharide, respectively, is linked to glucose.

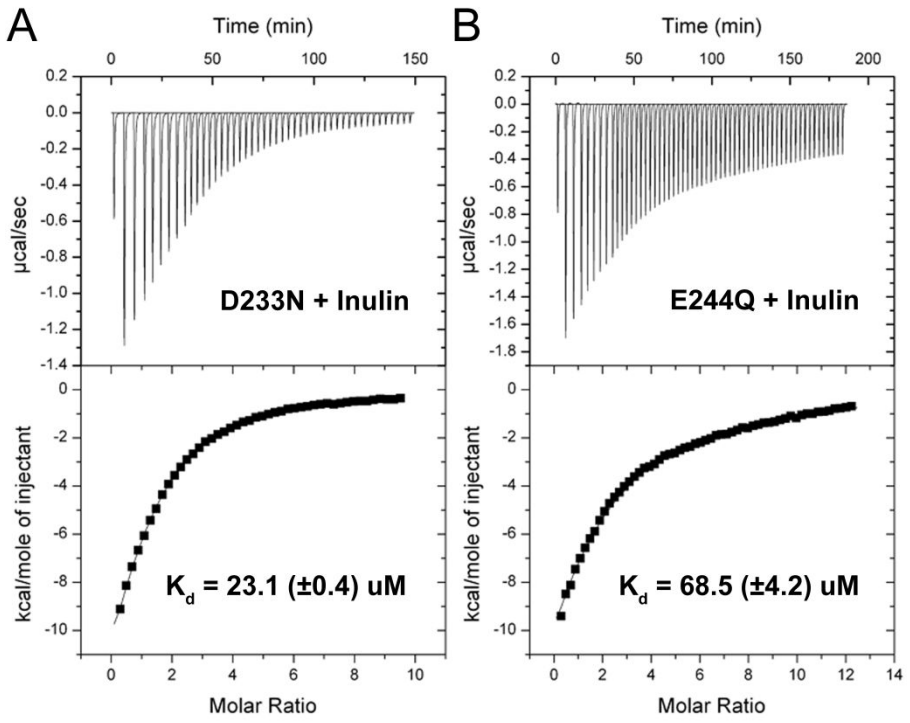

Figure 16. Isothermal titration calorimetric analysis. (A) Titration of inulin into D233N. (B) Titration of inulin into E244Q. The ITC measurements were carried out by titrating 5ul of 2 mM inulin into 1.4 ml of 12.5 uM each mutant.

DISCUSSION

The X-ray crystal structure of BsIFTase reveals that it folds into a β-helix. The program BetaWrap (Cowen *et al*., 2002) successfully predicted a β-fold structure for BsIFTase, with a raw score of -19.93 and a *P* value of 3.1×10^{-4}. The basic structural features of BsIFTase are largely reminiscent of a β-helix. Using DALI server (Holm and Sander, 1998), a high level of structural similarity was found between monomeric BsIFTase and 17 other β-helix structures with *Z*-values greater than 10; the rmsd values for the equivalent Cα atoms were 2.2 to 3.3 Å, suggesting that the arrangements of basic structural units are well conserved within these β-helical structures. Nonetheless, helical turns in the BsIFTase β-helix consist of two to four parallel β-strands. In other β-helix structures, a uniform number of β-strands, typically three β strands in each turn, is usually observed (Jenkins and Pickersgill, 2001; Jurnak *et al*., 1994; Jurnak and Yoder, 1995).

The most noticeable structural feature of BsIFTase is its oligomerization state, which is functionally and structurally essential for catalysis. The active sites in all known β-helix protein structures are located exclusively in the elongated groove parallel to the helical axis on the surface

between T3 and PB1 within a monomer (Jenkins and Pickersgill, 2001), implying that oligomerization is not essential for catalysis in these enzymes. Indeed, most of the β-helix enzymes characterized to date function as monomers. TSP, which forms a trimer in a manner similar to that of BsIFTase, is the exception, although its proposed catalytic mechanism occurs within a monomeric structural context (Steinbacher *et al*., 1996). Therefore, trimerization of the TSP β-helix may not be required for catalysis, and might instead be important for thermo-stability and protease resistance (Kreisberg *et al*., 2002; Simkovsky and King, 2006). In previous paper, as similar to that of TSP, several DFA-III-producing IFTases were also reported to be thermo-stable in high temperature up to 60°C, but rapidly inactivated at 70°C with short half-life (Kim *et al*., 2007; Zhao *et al*., 2011). As well, the pH stability of recombinant BsIFTase was peculiarly revealed in wider range between pH 5.0 to pH 10.0 than the native IFTase (Kim *et al*., 2007). Therefore, these studies of TSP and BsIFTase is supported that the trimerization of β-helix structures leads to the stability of proteins against a general harsh environment, like as high temperature, high pH and attack by protease. In contrast to that of TSP, the BsIFTase active site is located at the monomer-monomer interface. This structural feature is unprecedented for β-helical proteins, and implies that trimerization, which brings the catalytic residues together in the active site, is

a prerequisite for catalytic activity. These structural features are consistent with the results from analytical ultracentrifugation and site-directed mutagenesis studies (Figs. 6 and 14). In addition to BsIFTase, other IFTases have also yielded size-exclusion chromatography results that suggest a dimeric or trimeric structure (Kang *et al*., 1998; Haraguchi *et al*., 2003).

Another structural feature of BsIFTase is the size and shape of the substrate-binding pocket. The current structural evidence clearly reveals that the active site without the exit side is just large enough to accommodate one molecule of difructosaccharide in the pocket. From a structural perspective, therefore, a plausible mechanism for BsIFTase is that it successively removes the terminal difructosaccharide units of inulin as cyclic anhydrides. Hence, these structural data provide a physical basis for the exolytic activity of BsIFTase. These structural findings are analogous to those associated with cellobiohydrase CbhA of GH family 9 (Schubot *et al*., 2004). CbhA is a seven-module enzyme that shares many structural features with other GH9 members that exhibit endocellulase activity; in these other enzymes, a tunnel-shaped active site catalyzes endolytic cleavage of the substrate. However, the presence of a unique loop at one end of the tunnel in CbhA causes the active site exit to be blocked, and thus provides a structural basis for the exclusive exocellulase activity of CbhA. Taken together, these data of the structural features of

BsIFTase described here reveal many important features of the enzyme, including its functional trimerization, its exolytic mode of action, and the location of the active site at the monomer-monomer interface.

To date, mechanistic clues about IFTase- mediated catalysis, such as the identity of the active site residues and a possible mechanism for intramolecular fructosyl transfer, remain elusive. Although classified as a hydrolase by CAZy, BsIFTase does not have a pair of acidic residues in the vicinity of a possible glycosidic bond-cleavage site between subsite +1 and −1. The absence of a putative nucleophile and a general acid in this subsite precludes the idea of BsIFTase catalyzing the reaction in a manner similar to that of GHs typically employing two acidic residues (Davies and Henrissat, 1995). Instead, these structural and functional analysis suggests that BsIFTase catalyzes an intramolecular fructosyl transfer analogous to that of glycosyltransferases with an inverting mechanism (Tarbouriech *et al*., 2001; Coutinho *et al*., 2003).

Glycosyltransferases consist of two homologous β/α/β domains, and the active site is located in the crevice between the two domains (Coutinho *et al*., 2003). Therefore, neither the overall structure nor the active-site arrangement of BsIFTase bears any resemblance to those of glycosyltransferases. The generally accepted explanation for enzymatic

glycosyl transfer using the inverting mechanism is that the reaction is carried out using an S_N2-like single-displacement mechanism, in which the acceptor molecule is activated for nucleophilic attack by a general base. The resulting deprotonated acceptor can then attack at the anomeric center of the donor from the opposite side, with concomitant elimination of the moiety attached to the anomeric carbon of the donor. This attack results in inversion of the anomeric configuration at donor and forms a nascent covalent linkage between the donor and acceptor. In fact, x-ray crystallographic structure of DFA-III, a product by IFTase, indicated that one of fructose unit forms α-configuration on its anomeric center (Taniguchi and Uchiyama, 1982), suggesting that there is an inversion of the anomeric center, consistent with the inverting mechanism.

By analogy with the above mechanistic view, BsIFTase is proposed to catalyze the reaction *via* the inverting mechanism (Fig. 17). The terminal fructosyl unit F1 (subsite +2) bound at the inner site in BsIFTase appears to serve as the acceptor, and the F2 close to the entrance (subsite +1) might serve as the donor, given that the remaining fructose units of inulin containing the glucosyl end are expected to be eliminated as a leaving group upon catalysis. Therefore, the F2 fructosyl unit should undergo inversion of its anomeric configuration. Notably, the carboxylate group of Glu244 is within 2.6 Å of the O-3' hydroxyl group of F1 in this structure (Fig. 14), which immediately

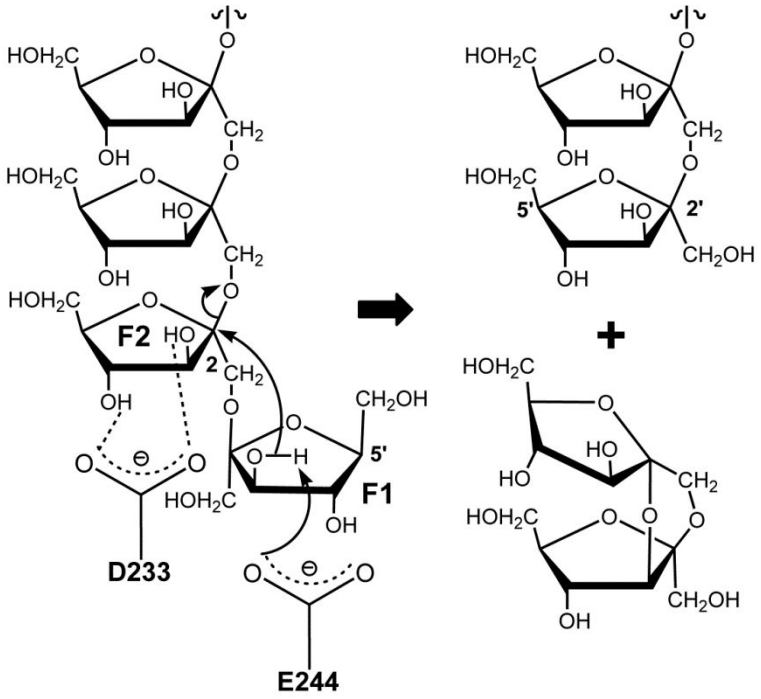

Figure 17. Proposed catalysis by BsIFTase. Details for the mechanism are described in text.

suggests that Glu244 acts as a general base to activate the acceptor. This suggestion is supported by the effect of the E244Q mutation, which essentially inactivates the enzyme (Fig. 15). These structural features are quite similar to those of glycosyltransferase employing an inverting mechanism in that the general base is exclusively either aspartate or glutamate (Tarbouriech *et al*., 2001; Coutinho *et al*., 2003), and recently a histidine residue activated by a nearby aspartate (Shao *et al*., 2005; Offen *et al*., 2006). Effect of Asp233 mutation is rather complicate. Apparently, Asp233 is involved in recognizing a donor F2 *via* hydrogen bonds (Fig. 14), and the measured binding affinity of inulin to D233N was almost similar to that of E244Q (Fig. 16). But a mutation of Asp233 eliminated catalytic activity (Fig. 15), suggesting that Asp233 plays a critical role in catalysis. Given that Asp233 is the only residue to directly interact with F2 unit, it might be one of possible roles by Asp233 to orient a donor F2 molecule into an optimal configuration for catalysis (see below), such that the nucleophilic attack by the deprotonated O-3' of F1 can be achieved efficiently. Further experiments will be required to explicitly assign the functional role of Asp233. Interactions between negatively charged residues such as aspartate and glutamate, and sugar donor substrate were also observed in other glycosyltransferases, in which mutation of those negatively charged residues abolished catalytic activity (Shao *et al*., 2005; Offen *et al*.,

2006), as characterized in BsIFTase.

In the binding mode observed for disaccharide F1−F2, the perpendicular orientation of F2 relative to the F1 fructosyl unit appears to alleviate steric hindrance, thus allowing O-3' of acceptor F1 to more easily gain access to C-2 of donor F2. Although these two atoms are separated by about 5.5 Å, they are constrained by the pre-existing glycosidic bond between C-2' of F1 and O-1 of F2, resulting in an orientation of O-3' relative to C-2 that is unfavorable for an S_N2-like reaction (Fig. 14A). The dihedral angles involved in the 2'-1 glycosidic bond would therefore have to be adjusted in order for this nucleophilic attack to be achieved.

The proposed mechanism of BsIFTase is consistent with the results of this structural and functional analysis, which provided mechanistic insights into intramolecular fructosyl transfer. These insights cannot be extended to the homologous LFTase reaction, however. Since both fructosyl units in DFA-IV remain in the β-configuration, GH32 LFTases appear to carry out catalysis in a manner similar to that of the members of GH32, employing two acidic residues for catalysis, as well as a mechanism that forms the anhydride bond after cleavage of the β-2',6 glycosidic bond between subsite +1 and -1, and then results in retention of the anomeric configuration (Park *et al.*, 2012). To date, structural analyses for enzymes involved in fructan degradation and

biosynthesis in the GH32 (Alberto *et al*., 2004; Alberto *et al*., 2006; Nagem *et al*., 2004; Verhaest *et al*., 2005) and GH68 (Meng and Fütter, 2003; Martinez-fleites *et al*., 2005) families have resulted exclusively in five-bladed β-propeller structures. In contrast, the present study demonstrates that the structurally unrelated β-helix carries out an intramolecular fructosyl transfer in a way analogous to intermolecular glycosyl transfer by glycosyltransferases. The considerable level of sequence identity between members of the IFTase family suggests that these proteins function similarly to BsIFTase.

REFERENCES

Alberto, F., Bignon, C., Sulzenbacher, G., Henrissat, B., and Czjzek, M. (2004) The three-dimensional structure of invertase (β-Fructosidase) from *Thermotoga maritima* reveals a bimodular arrangement and an evolutionary relationship between retaining and inverting glycosidases. *J. Biol. Chem.* **279**, 18903-18910.

Alberto, F., Jordi, E., Henrissat, B., and Czjzek, M. (2006) Crystal structure of inactivated *Thermotoga maritima* invertase in complex with the trisaccharide substrate raffinose. *Biochem. J.* **395**, 457-462.

Brunger, A. T., Adams, P. D., Clore, G. M., DeLano, W. L., Gros, P., Grosse-Kunstleve, R. W., Jiang, J. S., Kuszewski, J., Nilgus, M., Pannu, N. S., Read, R. J., Rice, L. M., Simonson, T., and Warren, G. L. (1998) Crystallography & NMR System: A new software suite for macromolecular structure determination. *Acta Crystallogr. Sect. D Biol. Crystallogr.* **54**, 905-921.

Collaborative Computational Project Number 4 (1994) The CCP4 suite: programs for protein crystallography. *Acta Crystallogr. Sect. D Biol. Crystallogr.* **50**, 760-763.

Coutinho, P. M., Deleury, E., Davies, G. J., and Henrissat, B. (2003) An evolving hierarchical family classification for glycosyltransferase. *J. Mol. Biol.* **328**, 307-317.

Cowen, L., Bradley, P., Menke, M., King, J., and Berger, B. (2002) Predicting the Beta-helix fold from protein sequence data. *J. Comput. Biol.* **9**, 261-267.

Davies, G. J., and Henrissat, B. (1995) Structures and mechanisms of glycosyl hydrolases. *Structure* **3**, 853-859.

Davies, G. J., Wilson, W. S., and Henrissat, B. (1997) Nomenclature for sugar-binding subsites in glycosyl hydrolases. *Biochem. J.* **321**, 557-559.

Gouet, P., Courcelle, E., Stuart, D. I., and Metoz, F. (1999) ESPript: multiple sequence alignments in PostScript. *Bioinformatics* **15**, 305-308.

Haraguchi, K., Seki, K., Kishimoto, M., Nagata, T., Kasumi, T., Kainuma, K., and Kobayashi, S. (1995) Cloning and nucleotide sequence of the inulin fructotransferase (DFA I-producing) gene of *Arthrobacter globiformis S14-3*. *Biosci. Biotechnol. Biochem*. **59**, 1809–1812.

Haraguchi, K., Yoshida, M., and Ohtsubo, K. (2003) Purification and properties of a heat-stable inulin fructotransferase from *Arthrobacter ureafaciens*. *Biotechnol. Lett.* **25**, 1049-1053.

Henrissat, B., and Davies, G. (1997) Structural and sequence-based classification of glycoside hydrolases. *Curr. Opin. Struct. Biol.* **7**, 637-644.

Herron, S. R., Benen, J. A. E., Scavetta, R. D., Visser, J., and Jurnak, F. (2000) Structure and function of pectic enzymes: Virulence factors of plant pathogen. *Proc. Natl. Acad. Sci. USA* **97**, 8762-8769.

Holm, L., and Sander, C. (1998) Touring protein fold space with Dali/FSSP. *Nucl. Acids. Res.* **26**, 316-319.

Jenkins, J., and Pickersgill, R. (2001) The architecture of parallel β-helices and related folds. *Prog. Biophys. Mol. Biol.* **77**, 111-175.

Jones, T. A., Zou, J. Y., Cowan, S. W., and Kjeldgaard, M. (1991) Improved methods for the building of protein models in electron density maps and the location of errors in these models. *Acta Crystallogr. Sect.* A **47**, 110-119.

Jurnak, F., Yoder, M. D., Pickersgill, R., and Jenkins, J. (1994) Parallel β-domains: a new fold in protein structures. *Curr. Opin. Struct. Biol.* **4**, 802-806.

Jurnak, F., and Yoder, M. D. (1995) The parallel β helix and other coiled folds. *FASEB J.* **9**, 335-342.

Kang, S. I., Kim, W. P., Chang, Y. J., and Kim, S. I. (1998) Purification and properties of inulin fructotransferase (DFA III-producing) from *Bacillus sp. snu-7 Biosci. Biotechnol. Biochem.* **62**, 628-631.

Kim, C. H., Jang, E. K., Kim, S. H., Jang, K. H., Kang, S. A., Song, K. B., Kwon, O. S., and Rhee, S. K. (2005) Molecular cloning of levan

fructotransferase gene from *Arthrobacter ureafaciens* K2032 and its expression in *Escherichia coli* for the production of difructose dianhydride IV. *Lett. Appl. Microbiol.* **40**, 228-234.

Kim, C. S., Hong, C. K., Kim, K. Y., Wang, X. L., Kang, S. I., and Kim, S. I. (2007) Cloning, expression, and characterization of *Bacillus sp. snu-7* inulin fructotransferase. *J. Microbiol. Biotechnol.* **17**, 37-43.

Kim, K. Y., Rhee, S., and Kim, S. I. (2005) Role of the N-terminal domain of endoinulinase from *Arthrobacter sp.* S37 in regulation of enzyme catalysis. *J. Biochem.* **138**, 27-33.

Knott, G. D. (1979) MLAB – a mathematical modeling tool. *Comput. Programs. Biomed.* **10**, 271-280.

Kreisberg, J. F., Betts, S. D., Haase-Pettingell, C., and King, J. (2002) The interdigitated β-helix domain of the P22 tailspike protein acts as a molecular clamp in trimer stabilization. *Protein Sci.* **11**, 820-830.

Larsson, A. M., Andersson, R., Stahlberg, J., Kenne, L., and Jones, T. A. (2003) Dextranase from *Penicillium minioluteum*: reaction course, crystal structure, and product complex. *Structure* **11**, 1111-1121.

Laue, T. M., Shah, B., Ridgeway, T. M., and Pelleitier, S. L. (1992) Computer-aided interpretation of analytical sedimentation data for proteins. Analytical

Ultracentrifugation in Biochemistry and Polymer Science, Royal Soiety of Chemistry, Cambridge, 90-125.

Martinez-fleites, C., Ortiz-lombardia, M., Pons, T., Tarbouriech, N., Taylor, E. J., Arrieta, J. G., Hernandez, L., and Davies, G. J. (2005) Crystal structure of levansucrase from the gram-negative bacterium *Gluconacetobacter diazotrophicus*. *Biochem. J.* **390**, 19-27.

Matteo, A. D., Giovane, A., Raiola, A., Camardella, L., Bonivento, D., De Lorenzo, G., Cervone, F., Bellincampi, D., and Tsemoglou, D. (2005) Structural basis for the interaction between pectin methylesterase and a specific inhibitor protein. *Plant Cell* **17**, 849-858.

Meng, G., and Fütterer, K. (2003) Structural framework of fructosyl transfer in *Bacillus subtilis* levansucrase. *Nat. Struct. Biol.* **10**, 935-941.

Michel, G., Helbert, W., Kahn, R., Dideberg, O., and Kloareg, B. (2003) The structural bases of the processive degradation of ι-Carrageenan, a main cell wall polysaccharide of red algae. *J. Mol. Biol.* **334**, 421-433.

Momma, M., Fujimoto, Z., Maita, N., Haraguchi, K., and Mizuno, H. (2003) Expression, crystallization and preliminary X-ray crystallographic studies of *Arthrobacter globiformis* inulin fructotransferase. *Acta Crystallogr. Sect. D Biol. Crystallogr.* **59**, 2286-2288.

Nagem, R. A. P., Rojas, A. L., Golubev, A. M., Korneeva, O. S., Eneyskaya, E. V., Kulminskaya, A. A., Neustroev, K. N., and Polikarpov, I. (2004) Crystal structure of exo-inulinase from *Aspergillus awamori*: The enzyme fold and structural determinants of substrate recognition. *J. Mol. Biol.* **344**, 471-480.

Offen, W., Martinez-Fleites, C., Yang, M., Kiat-Lim, E., Davis, B. G., Tarling, C. A., Ford, C. M., Bowles, D. J., and Davies, G. J. (2006) Structure of a flavonoid glucosyltransferase reveals the basis for plant natural product modification. *EMBO J.* **25**, 1396-1405.

Otwinowski, Z., and Minor, W. (1997) Processing of X-ray diffraction data collected in oscillation mode. *Methods Enzymol.* **267**, 307-326.

Park, J., Kim, M. I., Park, Y. D., Shin, I., Cha, J., Kim, C. H., and Rhee, S. (2012) Structural and functional basis for substrate specificity and catalysis of levan fructotransferase. *J. Biol. Chem*. **287**, 31233–31241.

Ritsema, T., and Smeekens, S. (2003) Fructans: beneficial for plants and humans. *Curr. Opin. Plant Biol.* **6**, 223-230.

Schubot, F. D., Kataeva, I. A., Chang, J., Shah, A. K., Ljungdahl, L. G., Rose, J. P., and Wang, B. (2004) Structural basis for the exocellulase activity of the cellobiohydrolase CbhA from *Clostridium thermocellum*. *Biochemistry* **43**, 1163-1170.

Shao, H., He, X., Achnine, L., Blount, J. W., Dixon, R. A., and Wang, X. (2005) Crystal structures of a multifunctional triterpene/flavonoid glycosyltransferase from *Medicago truncatula*. *Plant Cell* **17**, 3141-3154.

Simkovsky, R., and King, J. (2006) An elongated spine of buried core residues necessary for *in vivo* folding of the parallel β-helix of P22 tailspike adhesion. *Proc. Natl. Acad. Sci. USA* **103**, 3575-3580.

Steinbacher, S., Baxa, U., Miller, S., Weintraub, A., Seckler, R., and Huber, R. (1996) Crystal structures of phage P22 tailspike protein complexed with *Salmonella* sp. O-antigen receptors. *Proc. Natl. Acad. Sci. USA* **93**, 10584-10588.

Taniguchi, T., and Uchiyama, T. (1982) The crystal structure of di-fructose anhydride III, produced by inulin $_{D}$-fructotransferase. *Carbohydr. Res.* **107**, 255-262.

Tarbouriech, N., Charnock, S. J., and Davies, G. J. (2001) Three-dimensional structures of the Mn and Mg dTDP complexes of the family GT-2 glycosyltransferase SpsA: a comparison with related NDP-sugar glycosyltransferases. *J. Mol. Biol.* **314**, 655-66147.

Terwilliger, T. C., and Berendzen, J. (1999) Automated MAD and MIR structure solution. *Acta Crystallogr. Sect. D Biol. Crystallogr.* **55**, 849-861.

Terwilliger, T. C. (2000) Maximum-likelihood density modification. *Acta Crystallogr. Sect. D Biol. Crystallogr.* **56**, 965-972.

Van den Ende, W., De Coninck, B., and Van Laere, A., (2004) Plant fructan exohydrolases: a role in signaling and defense. *Trends Plant Sci.* **9**, 523-528.

van Hijum, S. A. F. T., van der Maarel, M. J. E. C., and Dijkhuizen, L. (2003) Kinetic properties of an inulosucrase from *Lactobacillus reuteri* 121. *FEBS Lett.* **534**, 207-210.

Van Riet, L., Nagaraj, V., Van den Ende, W., Clerens, S., Wiemken, A., and Van Laere, A. (2006) Purification, cloning and functional characterization of a fructan 6-exohydrolase from wheat (*Triticum aestivum* L.). *J. Exp. Bot.* **57**, 213-223.

van Santen, Y., Benen, J. A. E., Schröter, K., Kalk, K. H., Armand, S., Visser, J., and Dijkstra, B. W. (1999) 1.68-Å crystal structure of endopolygalacturonase II from *Aspergillus niger* and identification of active site residues by site-directed mutagenesis. *J. Biol. Chem.* **274**, 30474-30480.

Verhaest, M., Van den Ende, W., Le Roy, K., De Ranter, C. J., Van Laere, A., and Rabijns, A. (2005) X-ray diffraction structure of a plant glycosyl hydrolase family 32 protein: fructan 1-exohydrolase IIa of *Cichorium intybus*. *Plant J.* **41**, 400-411.

Vijn, I., and Smeekens, S. (1999) Fructan: more than a reserve carbohydrate? *Plant Physiol.* **120**, 351-359.

Yang, S. J., Park, N. H., Lee, T. H., and Cha, J. (2002) Expression, purification and characterization of a recombinant levan fructotransferase. *Biotechnol. Appl. Biochem.* **35**, 199-203.

Yoder, M. D., Keen, N. T., and Jurnak, F. (1993) New domain motif: the structure of Pectate lyase C, a secreted plant virulence factor. *Science* **260**, 1503-1507.

Zhao, M., Mu, W., Jiang, B., Hang, H., Zhou, L., and Zhang, T. (2011) Cloning and extracellular expression of inulin fructotransferase from *Arthrobacter aurescens SK 8.001* in *E. coli*. *J. Sci. Food Agric*. **91**, 2715-2721.

This paper was published in The Journal of Biological Chemistry in 2007 under the same title. Jung, W. S., Hong, C. K., Lee, S., Kim, C. S., Kim, S. J., Kim, S. I., and Rhee, S. (2007) Structural and functional insights into intramolecular fructosyl transfer by inulin fructotransferase. *J. Biol. Chem*. 282, 8414–8423.

CHAPTER II

Structural and Functional Analysis of Phytotoxin Toxoflavin-Degrading Enzyme

INTRODUCTION

Pathogenic bacteria employ an array of protein molecules and/or secondary metabolites as mediators of pathogenicity in human, animal, and plant hosts. In general, while bacterial molecules such as lipopolysaccharides, capsular polysaccharides, peptidoglycans, and lipoproteins serve as pathogen-associated molecular patterns to initiate interactions with the host, they also activate the host innate immune system (Chisholm *et al*., 2006; Trinchieri *et al*., 2007). To evade host defense systems, pathogens directly inject bacterial proteins, known as effectors, into the cytosolic compartment of host cells *via* various secretion systems (Galán, 2009), which have been well characterized in plant immune responses (Chisholm *et al*., 2006). Effectors play essential roles in pathogenesis by disturbing the metabolism of host cells through several different strategies (Galán, 2009; Mudgett, 2005; Block *et al*., 2008). In addition to these recently characterized processes, bacteria have also been shown to synthesize and secrete toxic low molecular weight chemicals, collectively called toxins, as virulence factors (Agrios, 2005). The modes of action, which are unique to each toxin, show great diversity in host cells and range from gene regulation to the control of ion channel activity (Agrios, 2005;

Möbius and Hertweck, 2009). Structural and single-molecule studies of toxins in complexes with target proteins have provided molecular insights into the functional roles of those toxins (Wurtele *et al*., 2003; Meiss *et al*., 2008).

In recent years, it has become evident that the expression of genes involved in the synthesis and secretion of toxins is regulated at the level of transcription by quorum sensing, the central mechanism for bacterial intercellular signaling that utilizes diffusible small chemicals as a signal (Schuster and Greenberg, 2006). This general theme is applicable to the phytopathogenic bacterium *Burkholderia glumae* BGR1, which is responsible for bacterial wilt in crop plants. *Burkholderia glumae* produces toxoflavin (Fig. 18; Nagamatsu, 2001), which acts as a key factor in this disease, possibly by producing superoxide and hydrogen peroxide (Latuasan and Berends, 1961; Nagamatsu *et al*., 1982). However, in recent researches as reverse acting, toxoflavin and its derivatives have been reported to inhibit SIRT1/2 enzymes involved in tumorigenesis and tyrosyl-DNA phosphodiesterase II enzyme, implicated in the topoisomerase-mediated repair of DNA damage, as an anticancer drug (Choi *et al*., 2013; Raoof *et al*., 2013). In fact, the synthesis and transport of toxoflavin in *B. glumae* were shown to be coordinately regulated by quorum sensing signals (Kim *et al*., 2004). The antivirulence strategy referred to as quorum quenching (Dong *et al*., 2007) has been

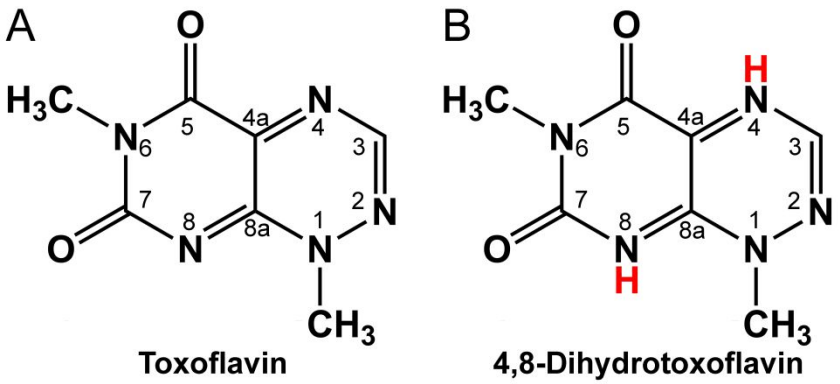

Figure 18. Chemical structure of toxoflavin and the derivative. The chemical structure of toxoflavin (A) and 4,8-dihydrotoxoflavin (B) is shown with the numbering of atoms.

suggested to disrupt quorum sensing by degrading *N*-acylhomoserine lactones (AHLs), the quorum sensing signals produced in many Gram-negative bacteria. For example, lactonases produced by some *Bacillus sp*. are known to hydrolyze the lactone bond in the homoserine ring of AHLs, and transgenic plants expressing *Bacillus* AHL lactonase showed resistance to quorum sensing-dependent bacterial infection (Dong *et al*., 2001). Recently, another type of quorum-quenching enzyme, PvdQ, was identified, and structural analysis indicated that this enzyme hydrolyzes the peptide bond between the acyl chain and homoserine ring of AHLs (Bokhove *et al*., 2010).

In addition to quorum quenching, degradation of the toxin itself could serve as an antivirulence strategy in toxin-mediated diseases. An enzyme that showed the ability to degrade toxoflavin *in vitro* was recently identified from *Paenibacillus polymyxa JH2* and was named toxoflavin-degrading enzyme (TxDE) (Koh *et al*., 2010). Although the *in vivo* function of TxDE in *P. polymyxa JH2* remains to be determined, its identification and characterization may contribute significantly to plant biotechnology by providing a non-antibiotic selection marker for plants (Koh *et al*., 2010). Furthermore, this may lead to the development of disease-resistant crops carrying an antivirulence factor to prevent bacterial wilt. Despite the biotechnological significance of TxDE, there have been no previous reports of its biochemical or structural

properties. To understand the structural and functional features of TxDE, it was determined that crystal structure in substrate-free form and in complex with the substrate toxoflavin, and performed further functional analysis of the active site residues. These results provide molecular insight into catalysis by the enzyme, its proposed role as a non-antibiotic selection marker for plants, and its function as an antivirulence factor in toxoflavin-mediated plant diseases.

MATERIALS AND METHODS

1. Construction of TxDE variants

For structural and functional analysis, various TxDE enzymes were produced as described below. The DNA fragment of TxDE was amplified from cDNA of *Paenibacillus polymyxa JH2* (Koh *et al*., 2010) (GenBank accession number GQ921834) by PCR with sequence specific and/or mutagenic primers. The resulting PCR products were ligated into the *Nde*I and *Xho*I sites of the expression vector pET41b containing a C-terminal His-tag. Since a wild-type TxDE failed to produce a crystal for structural analysis, extensive search has been carried out to identify TxDE mutants suitable for further structural study. Among those mutant enzymes produced, TxDE(F94S) successfully yielded a crystal for the initial structural analysis. Subsequently, the TxDE(D175A) mutant was used for further structural analysis of the substrate-free form and the complex with the substrate toxoflavin.

2. Expression, purification, and crystallization

Escherichia coli BL21(DE3) *pLys*S strain (Stratagene) harboring the plasmid was used to express the C-terminal His-tagged TxDE protein. Cells were grown at 37°C in Luria-Bertani medium containing 10 mg/L kanamycin

and 34 mg/L chloramphenicol to an OD_{600} of 0.8, and then induced at 37°C for 4 h with the addition of 1 mM isopropyl-1-thio-β-$_D$-galactopyranoside. The harvested cells were sonicated in buffer A (50 mM Tris-HCl, pH 7.5, 200 mM NaCl, 1 mM DTT, and 1 mM $MnCl_2$) and subjected to centrifugation at 30,000 ×g for 1 h. The crude extract was applied to a HisTrap column (GE Healthcare), and TxDE protein was eluted using buffer B (buffer A plus 500 mM imidazole). After dialysis against buffer C (50 mM Tris-HCl, pH 7.5, 1 mM DTT, and 1 mM $MnCl_2$), the protein was further purified using a Mono-Q column (GE Healthcare) with a linear gradient of NaCl. After dialysis against buffer C, the enzyme was concentrated to about 12 mg/mL for crystallization. A SeMet-substituted TxDE(F94S) protein was prepared as described above, except that the expression plasmid was transformed into E. coli strain B834(DE3) *pLys*S, a methionine auxotroph (Novagen), and the protein was expressed in minimal medium in the presence of 10 mg/mL SeMet.

Crystallization was carried out at 22°C using the sitting-drop vapor-diffusion method. Crystals of TxDE(F94S) were produced with buffer containing of 0.1 M MES, pH 6.5, 50 mM $CaCl_2$, 28% (v/v) PEGMME5000, and 0.1 M NaI, whereas TxDE(D175A) crystals were produced under the following conditions: 0.1 M CAPS, pH 10.5, 0.2 M $LiSO_4$, and 1.2 M NaH_2PO_4/0.8 M K_2HPO_4 (Fig. 19).

Figure 19. Crystals of His-tagged TxDE. Crystals of TxDE(F94S) for MAD were produced with buffer containing of 0.1 M MES, pH 6.5, 50 mM $CaCl_2$, 28% (v/v) PEGMME5000, and 0.1 M NaI, whereas TxDE(D175A) crystals of this figure were confirmed under the following different conditions: 0.1 M CAPS, pH 10.5, 0.2 M $LiSO_4$, and 1.2 M NaH_2PO_4/0.8 M K_2HPO_4.

3. Data collection and structure determination

In general, crystals of SeMet-TxDE(F94S) and TxDE(D175A) were soaked in the respective crystallization mother solution with the addition of the appropriate cryoprotectant (see below) as well as ligand, as necessary, and then flash-frozen in liquid nitrogen. For structure determination by multi-wavelength anomalous dispersion, data using a SeMet-TxDE(F94S) crystal were collected at three different wavelengths to 2.2 Å resolution at 100 K. Later, single-wavelength data were also obtained using crystals of TxDE(D175A) to 1.6 Å resolution and the complex with toxoflavin at 2.0 Å resolution, respectively, on beamlines 4A and 6C at Pohang Accelerator Laboratory, Pohang, Korea (Fig. 20). All crystals had the symmetry of the space group *R3*; however, owing to different cell parameters, there were four monomers and one monomer in an asymmetric unit for TxDE(F94S) and TxDE(D175A) crystals, respectively. Collected data were processed using the HKL2000 package (Otwinowski and Minor, 1997) (Table 3).

Glycerol was initially used as a cryoprotectant in structural analysis of SeMet-TxDE(F94S) crystals. However, preliminary data indicated preferential binding of glycerol to the active site; therefore, either sucrose or PEG4000 was used as an alternative cryoprotectant in the structural analysis of TxDE(D175A) crystals. Specifically, the TxDE(D175A) crystal was soaked in

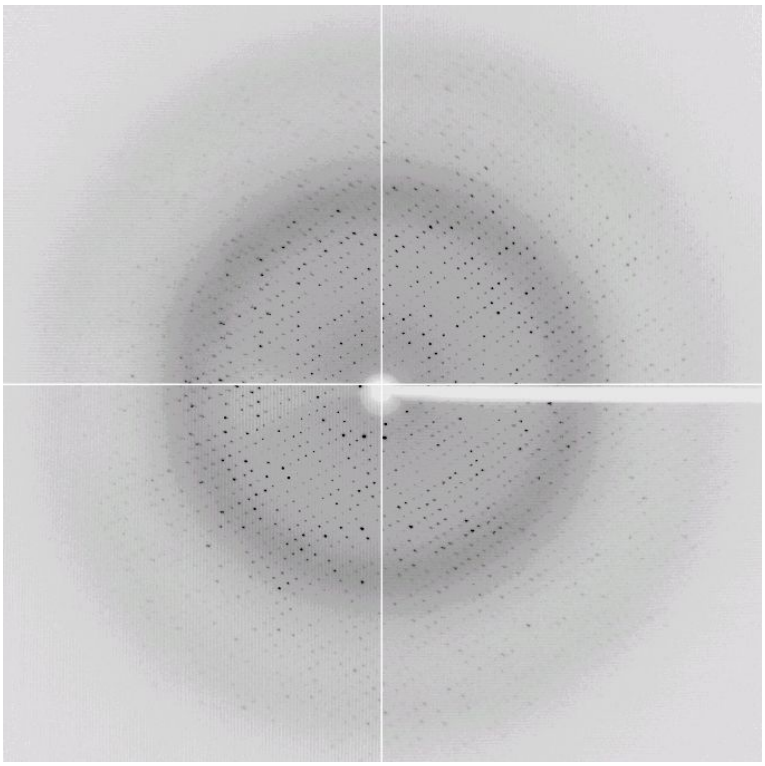

Figure 20. Diffraction of His-tagged TxDE crystal. A SeMet-TxDE(F94S) crystal were collected at 2.2 Å resolution on beamline 4A at Pohang Accelerator Laboratory, Pohang, Korea. The crystals belonged to the trigonal space group *R3*.

Table 3. Crystallographic data and refinement statistics for MAD (SeMet) structures.

	SeMet TxDE(F94S)			TxDE(D175A)	TxDE(D175A) -Tox
Data collection					
Space group	R3			R3	R3
Cell dimensions					
a, *b*, *c* (Å)	a = b = 214.703, c = 57.062			a = b = 110.377, c = 56.787	a = b = 111.008, c = 57.438
α, β, γ (°)	α = β = 90, γ = 120			α = β = 90 γ = 120	α = β = 90 γ = 120
	Peak	*Inflection*	*Remote*		
Wavelength	0.97948	0.97963	0.97179	1.2398	1.2398
Resolution (Å)	50.0-2.2 (2.28-2.2)			50.0-1.6 (1.66-1.6)	50.0-2.0 (2.03-2.0)
R_{sym} or R_{merge}[a]	7.6 (42.6)	6.1 (45.4)	7.0 (58.2)	6.4 (25.7)	7.2 (30.1)
$I / \sigma I$	34.2 (5.1)	34.9 (3.8)	27.9 (2.0)	30.9 (4.1)	28.0 (5.0)
Completeness (%)	96.9 (68.7)	96.9 (69.2)	98.8 (87.7)	98.5 (88.5)	100.0 (99.9)
Redundancy	11.1 (10.3)	7.7 (6.9)	7.5 (5.4)	6.1 (5.3)	6.3 (5.9)
Refinement					
Resolution (Å)	50.0-2.2			50.0-1.6	50.0-2.0
No. reflections	43,558 / 4371			30,441 / 3,030	15,929 / 1,552
R_{work}[b] / R_{free}[c]	24.9 / 31.0			19.5 / 22.0	21.9 / 25.7
No. atoms					
Protein	7,024			1,738	1,738
Ligand/ion					14
Water	159			134	102
Average *B*-factors (Å^2)					
Protein	36.3			22.7	25.8
Ligand/ion					32.5
Water	31.7			28.5	32.3
R.m.s deviations					
Bond lengths (Å)	0.007			0.010	0.009
Bond angles (°)	1.356			1.553	1.442
Ramachandran plot					
Favored (%)	81.6			88.3	89.8
Allowed (%)	18.2			11.2	9.7
Disallowed (%)	0.2			0.5[d]	0.5[d]

Values in parenthesis are for the highest resolution shell.

[a] $R_{merge} = \Sigma|I_h - \langle I_h \rangle| / \Sigma I_h$, where I_h is the observed intensity and $\langle I_h \rangle$ is the average intensity.

[b] $R_{work} = \Sigma||F_{obs}| - k|F_{cal}|| / \Sigma|F_{obs}|$.

[c] R_{free} is the same as R_{obs} for a selected subset (10%) of the reflections that was excluded from refinement.

[d] Gln-176 is in a disallowed region.

a solution of 0.1 M CAPS, pH 10.5, and 48% PEG4000 as cryoprotectant for the substrate-free structure. As toxoflavin becomes very labile at high pH (particularly above pH 9.5), an extensive search was carried out for the formation of the complex with toxoflavin. Later, it was found that the TxDE(D175A)-toxoflavin complex could be formed by soaking a TxDE(D175A) crystal for about 30 min in a solution of 0.1 M HEPES, pH 7.5, 2 M ammonium sulfate, 2% PEG400, and 20% sucrose, as well as additional 1 mM $MnCl_2$, 5 mM DTT, and 2 mM toxoflavin.

For TxDE(F94S) structure determination, the program SOLVE/RESOLVE (Terwilliger and Berendzen, 1999; Terwilliger, 2000) was used for initial phasing and density modification. The initial electron density map was sufficiently interpretable to trace all residues, except the N-terminal Met1 and the last two histidine residues in the C-terminal His-tag. The model was built using O (Jones *et al*., 1991) and refined using CNS (Brunger *et al*., 1998). The R_{work} and R_{free} of the TxDE(F94S) structure were 25% and 31%, respectively, after refinement using CNS. Later, data for TxDE(D175A) at 1.6 Å resolution were collected, and the structure was determined by molecular replacement using the program CNS, with a refined model of monomeric structure from TxDE(F94S) as a search model. Model building and refinement were carried out in a manner identical to that for TxDE(F94S). The structure

of the TxDE(D175A)–toxoflavin complex was also determined by molecular replacement using the program CNS, with a refined model of TxDE(F94S) as a search model. Currently, a structure of TxDE(D175A) and its complex with toxoflavin is refined to final R_{work}/R_{free} values of 19.5/22.0% and 21.9/25.7%, respectively, and no residues were found to be in a disallowed region in Ramachadran plot, except for Gln176 (Fig. 21). Details of the refinement are listed in Table 3.

The atomic coordinates and structure factors (codes 3OUL for the substrate-free form of TxDE(D175A), 3OUM for its complex with toxoflavin) have been deposited in the Protein Data Bank (http://www.rcsb.org).

4. Functional analysis

An enzyme assay to measure the degradation of toxoflavin was performed according to previously reported procedures (Koh *et al*., 2010). TxDE mutants for functional studies were prepared from wild-type TxDE gene in pET41b vector with mutagenic primers (Table 4), and their sequences were confirmed by DNA sequencing. All enzymes used were expressed and purified as described above, and their reactions were performed at 25°C under aerobic conditions, unless otherwise specified. Briefly, 400 mL of assay buffer (50 mM sodium phosphate, pH 7.0) contained 20 μL of TxDE enzyme (3

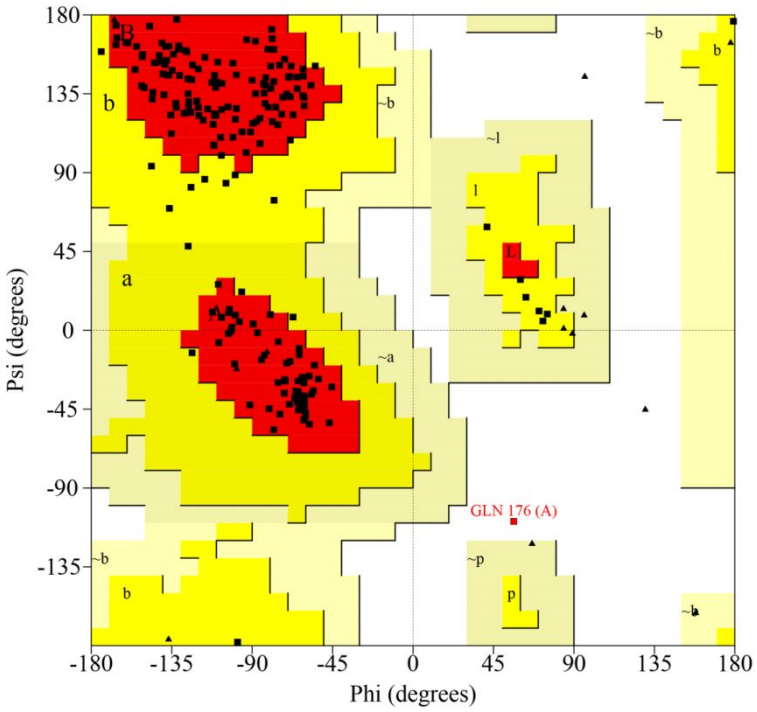

Figure 21. The Ramachandran plot of TxDE(D175A) structure. One residue Gln176 contained to disallowed region. Glycine residues are separately distinguished by triangles, which are not restricted to the regions of the plot for the other amino-acid side chains.

Table 4. Primer sequences of mutants.

E138A	
Forward	5’-CTACTAAGCATCGGTGCGATTAATATAACAACCAGCG-3’
Reverse	5’-CGCTGGTTGTTATATTAATCGCACCGATGCTTAGTAG-3’
E113A	
Forward	5’-GTCTGGTAATATTATTGCACTCATCTCGCGTCAGC-3’
Reverse	5’-GCTGACGCGAGATGAGTGCAATAATATTACCAGAC-3’
H60A	
Forward	5’-GAACAAAGCCCTTTTACGCTATTGCTATCAATATCGCGGC-3’
Reverse	5’-GCCGCGATATTGATAGCAATAGCGTAAAAGGGCTTTGTTC-3’
Y103F	
Forward	5’-CGCGTACTCCTGTTTTGTAGAAGACCCGTCTGG-3’
Reverse	5’-CCAGACGGGTCTTCTACAAAACAGGAGTACGCG-3’
F94W	
Forward	5’-GATCAGGCATACTGGCCCTTCTTTAACGCGTACTC-3’
Reverse	5’-GAGTACGCGTTAAAGAAGGGCCAGTATGCCTGATC-3’
L190G	
Forward	5’-GACGACGCTGGGGATTTTCAGAACGCGTAGC-3’
Reverse	5’-GCTACGCGTTCTGAAAATCCCCAGCGTCGTC-3’
L190P	
Forward	5’-GACGACGCTGGCCATTTTCAGAACGCGTAGC-3’
Reverse	5’-GCTACGCGTTCTGAAAATGGCCAGCGTCGTC-3’

mg/mL), 50 μM toxoflavin, 10 μM $MnCl_2$, and 5 mM DTT. After a 30-min incubation, an equal volume of chloroform was added to the assay buffer to stop the reaction. The resulting chloroform fraction was dried completely and then solubilized in 10 mL of methanol. Thin-layer chromatography was performed, and the degradation of toxoflavin was visualized under UV light at 365 nm.

For the enzyme reaction under anaerobic conditions, all processes were carried out in an anaerobic chamber filled with N_2 (MO Tek, Korea). Specifically, the reagent solutions were prepared in the chamber, and the protein solution was degassed before transport to the chamber. For the reactions in the absence of DTT or Mn^{2+} (Fig. 22), the purified enzyme was first extensively dialyzed against a buffer of 50 mM Tris, pH 7.5, and 10 mM EDTA, and then dialyzed again against 50 mM Tris buffer (pH 7.5).

5. ^{1}H-NMR study

Pure toxoflavin (Yoneda and Nagamatsu, 1973), 4,8-dihydrotoxoflavin (Nagamatsu, 2010), DTT, and 1,2-dithiane-4,5-diol (DTD) (Lee and Kohn, 2003) at a concentration of 10% in 99% deuterated methanol (CD_3OD) were measured as the authentic compounds. The spectra (A) to (C) of Figure 23 show the peak assignments for each proton in toxoflavin, 4,8-

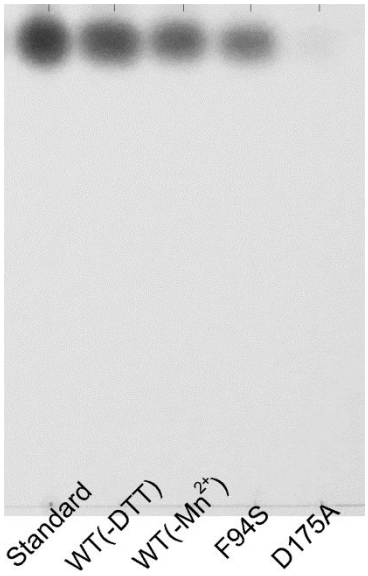

Figure 22. Thin-layer chromatographic analysis of toxoflavin degradation under various conditions. The enzyme reaction was carried out using three different enzymes: wild-type enzyme (WT), TxDE with the F94S mutation, and TxDE with the mutation D175A. For the reaction in the absence of DTT or Mn^{2+}, the purified WT enzyme was dialyzed against buffer in the presence of 10 mM EDTA, and then DTT or Mn^{2+} was added. The "Standard" lane is toxoflavin in the absence of any other components. Toxoflavin was degraded by D175A mutant enzymes, but not by the F94S mutant enzyme, as well as in the absence of DTT or Mn^{2+}. All reactions were carried out under aerobic conditions.

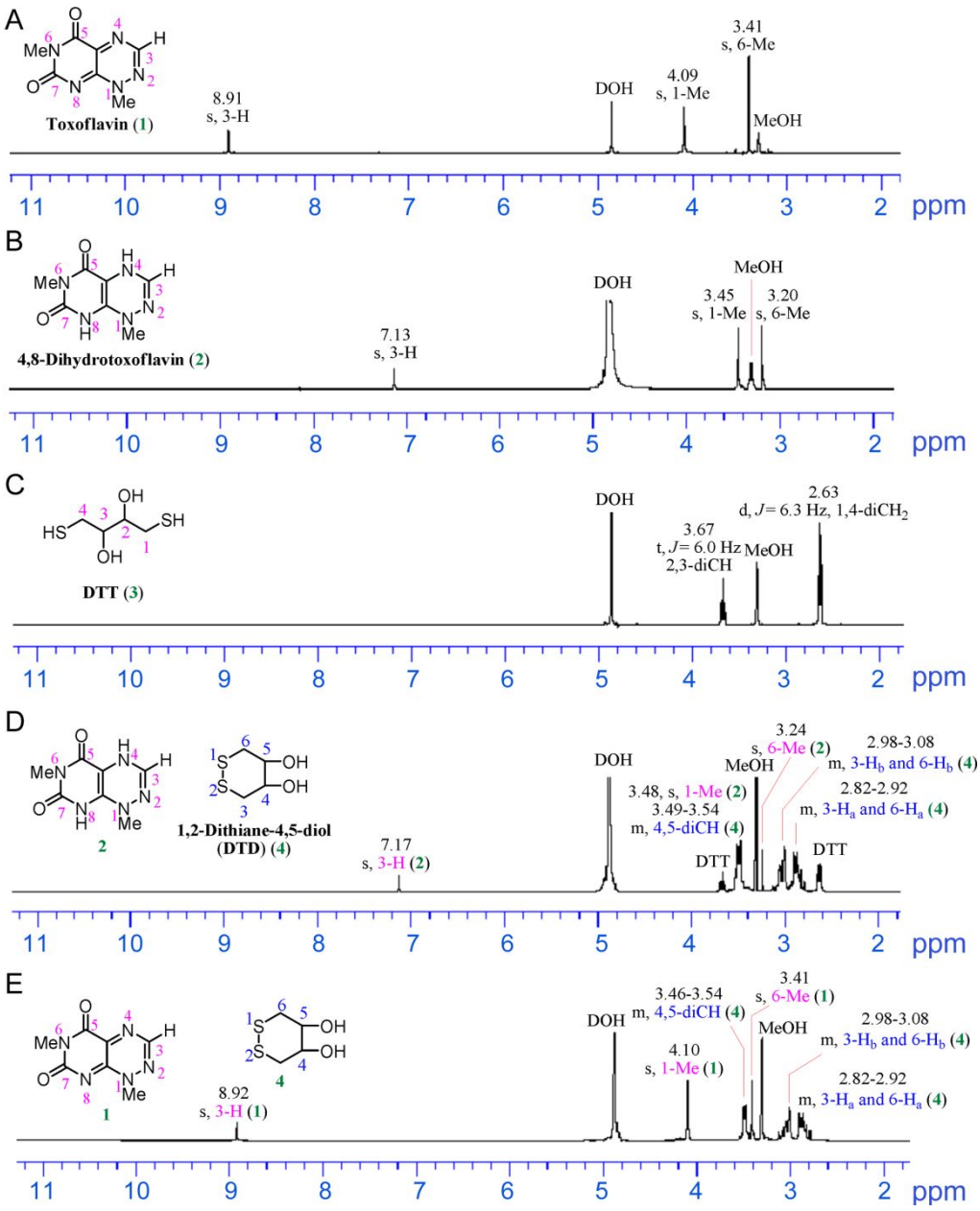
A
Toxoflavin (1)
8.91
s, 3-H
DOH
4.09
s, 1-Me
3.41
s, 6-Me
MeOH
B
4,8-Dihydrotoxoflavin (2)
7.13
s, 3-H
DOH
3.45
s, 1-Me
MeOH
3.20
s, 6-Me
C
DTT (3)
DOH
3.67
t, J= 6.0 Hz
2,3-diCH
MeOH
2.63
d, J= 6.3 Hz, 1,4-diCH2
D
2
1,2-Dithiane-4,5-diol
(DTD) (4)
7.17
s, 3-H (2)
DOH
3.24
s, 6-Me (2)
MeOH
2.98-3.08
m, 3-Hb and 6-Hb (4)
3.48, s, 1-Me (2)
3.49-3.54
m, 4,5-diCH (4)
2.82-2.92
m, 3-Ha and 6-Ha (4)
DTT
DTT
E
1
4
8.92
s, 3-H (1)
DOH
3.46-3.54
m, 4,5-diCH (4)
4.10
s, 1-Me (1)
3.41
s, 6-Me (1)
MeOH
2.98-3.08
m, 3-Hb and 6-Hb (4)
2.82-2.92
m, 3-Ha and 6-Ha (4)
11 10 9 8 7 6 5 4 3 2 ppm

Figure 23. ^{1}H-NMR experiments in deuterated methanol (99% CD_3OD). ^{1}H-NMR chemical shifts under aerobic conditions at 22°C for (A) pure toxoflavin (**1**), (B) pure 4,8-dihydrotoxoflavin (**2**), and (C) pure DTT (**3**) are shown with peak assignments for each proton in the compounds. (D) The ^{1}H-NMR experiment was performed in deuterated methanol after a 10-min reaction of toxoflavin (**1**) with an equimolar amount of DTT (**3**) at 22°C under aerobic conditions. A chemical shift analysis indicated that the reaction mixture contained predominantly 4,8-dihydrotoxoflavin (**2**) and DTD (**4**) with a small quantity of DTT (**3**), consistent with the results of the UV-Vis spectroscopic analysis shown in Figure 24. (E) After the reaction of toxoflavin (**1**) with an equimolar amount of DTT (**3**) in deuterated methanol at 22°C for 10 min under aerobic conditions, oxygen was bubbled into the reaction mixture for 1 min. The analysis indicated that all DTT (**3**) was converted into DTD (**4**) and 4,8-dihydrotoxoflavin (**2**) was converted into toxoflavin (**1**) by oxidation, again consistent with the results of the UV-Vis spectroscopic analysis shown in Figure 24. These experiments were performed by Ma, J., and Nagamatsu, T. in Okayama University.

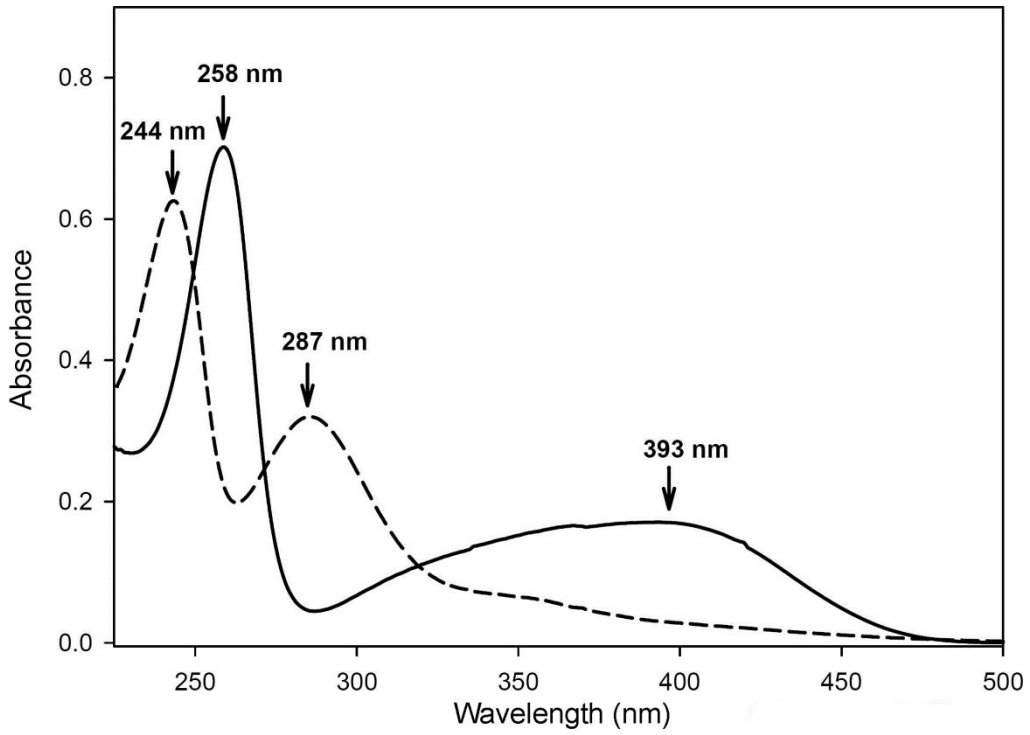
258 nm
244 nm
287 nm
393 nm
Absorbance
Wavelength (nm)
0.0
0.2
0.4
0.6
0.8
250
300
350
400
450
500

Figure 24. UV-Vis absorption spectra of toxoflavin in the absence and presence of DTT. Two different absorption spectra of toxoflavin (25 μM), which was dissolved in 50 mM HEPES, pH 6.8, and 10 μM $MnCl_2$, were recorded under aerobic conditions. In the absence of DTT (solid line), toxoflavin exhibits two absorption peaks, at 258 and 393 nm. Upon the addition of 2 mM DTT (dashed line), two peaks appeared, at 244 and 287 nm. The absorption peak at 287 nm corresponds to that of the oxidized form of DTT (*i.e.*, 1,2-dithiane-4,5-diol; DTD), and its absorbance varies according to the concentration of DTT used in the experiment. The peak at 244 nm was later identified by NMR spectroscopy as that of reduced toxoflavin (*i.e.*, 4,8-dihydrotoxoflavin) (Fig. 23); it remained stable only in the presence of DTT. After the DTT was exhausted, the spectrum of 4,8-dihydrotoxoflavin changed into that of toxoflavin (solid line) owing to oxidation by adventitious air or bubbled oxygen, with an additional absorbance shoulder at 287 nm for DTD. At this stage, toxoflavin was no longer degraded by the TxDE enzyme, unless additional DTT was added to the reaction mixture, strongly suggesting that the reduced form of toxoflavin is the true substrate for the enzyme.

toxoflavin, and DTT, respectively. The reaction was carried out in NMR tubes with an internal diameter of 5 mm under aerobic conditions at 22°C, and all spectra were measured in 99% CD_3OD. A mixture of toxoflavin (5 mg, 0.026 mmol) and (±)-DTT (4 mg, 0.026 mmol) in 99% CD_3OD (5 mL) was left to stand for 10 min. Then, the spectrum of the mixture was measured at 22°C (Fig. 7D). After oxygen was bubbled into the reaction mixture for 1 min, the spectrum of the mixture was obtained (Fig. 23E).

The following are the ^{1}H-NMR (in CD_3OD) data for toxoflavin: δ 3.41 (3H, s, 6-Me), 4.09 (3H, s, 1-Me), 8.91 (1H, s, 3-H); for 4,8-dihydrotoxoflavin: δ 3.20 (3H, s, 6-Me), 3.45 (3H, s, 1-Me), 7.13 (1H, s, 3-H); for DTT: δ 2.63 (4H, δ, $J_{1,2}$=$J_{3,4}$=6.3 Hz, 1- and 4-CH_2), 3.67 (2H, t, J=6.0 Hz, 2- and 3-CH); for 1,2-dithiane-4,5-diol: δ 2.82–2.92 (2H, m, 3-H_a and 6-H_a), 2.98–3.08 (2H, m, 3-H_b and 6-H_b), 3.46–3.54 (2H, m, 4- and 5-H).

RESULTS

1. Overall structure of TxDE

TxDE mutants have been extensively searched for suitable for structural study, because a wild-type enzyme failed to produce a crystal. Among those mutant enzymes, TxDE(F94S) successfully yielded a crystal for the initial structural analysis. The structure of TxDE was determined at 2.2 Å resolution using a crystal of selenomethionine (SeMet)-substituted TxDE(F94S) mutant enzyme (Table 3). However, the replacement of Phe-94 with a serine caused the enzyme to be catalytically inactive (Fig. 22), possibly by hindering the binding of substrate. Subsequently, the TxDE(D175A) mutant, which is catalytically active (Fig. 22), was crystallized. Its structure was determined in substrate-free form at 1.6 Å and in a binary complex with the substrate toxoflavin at 2.0 Å resolution, by molecular replacement with the refined structure of TxDE(F94S) as a search model (Table 3). These two structures have one monomer in an asymmetric unit. The structural features described in the present study are based on the structural analysis of TxDE(D175A).

TxDE encodes 221 residues, but a total of 222 residues from Thr-2 to the extraneous leucine and glutamine at the C-terminus form 14 β-strands and

three α-helices in the substrate-free form (Fig. 25). The topology of TxDE is composed mainly of two layers of β-sheets, which bisect the molecule into A- and B-domains, each with seven β-strands (Fig. 26). Specifically, the A-domain (residues 1–51 and 200–221) contains one βαβββ motif for the N-terminal 51 residues and one βββ motif for the C-terminal residues (Fig. 25). The strands in the A-domain are arranged in a mixed orientation, such that the β1 strand of the N-terminal $\beta1^{+}\ \beta4^{+}\ \beta3^{-}\ \beta2^{+}$ motif (the superscripts + and – indicate parallel or antiparallel orientation relative to the β1 strand) makes edge-to-edge contacts in an antiparallel manner with the β12 strand of the C-terminal $\beta12^{-}\ \beta13^{+}\ \beta14^{-}$ motif, resulting in a continuous seven-stranded β-sheet with a distorted orientation (Fig. 26). The only α-helix in the A-domain, α1, is located at the inner wall of the β-sheet, close to β2 and β3. A similar configuration, but with much greater distortion of the β strands, was observed in the B-domain (residues 58–186), which is connected to the A-domain by a long loop between β4 and β5, and between β11 and β12. Strands from β5 to β8 and helix α2 constitute a βαβββ motif, whereas three strands, β9 to β11, and helix α3 form a βαββ motif. Similar to the A-domain, two β strands in the B-domain, one from each motif (i.e., β5 and β9), interact with each other in an edge-to-edge orientation, such that seven strands in two motifs are arranged in the spatial order $\beta6^{+}\ \beta7^{-}\ \beta8^{+}\ \beta5^{+}\ \beta9^{-}\ \beta11^{-}\ \beta10^{+}$. The two motifs in the B-

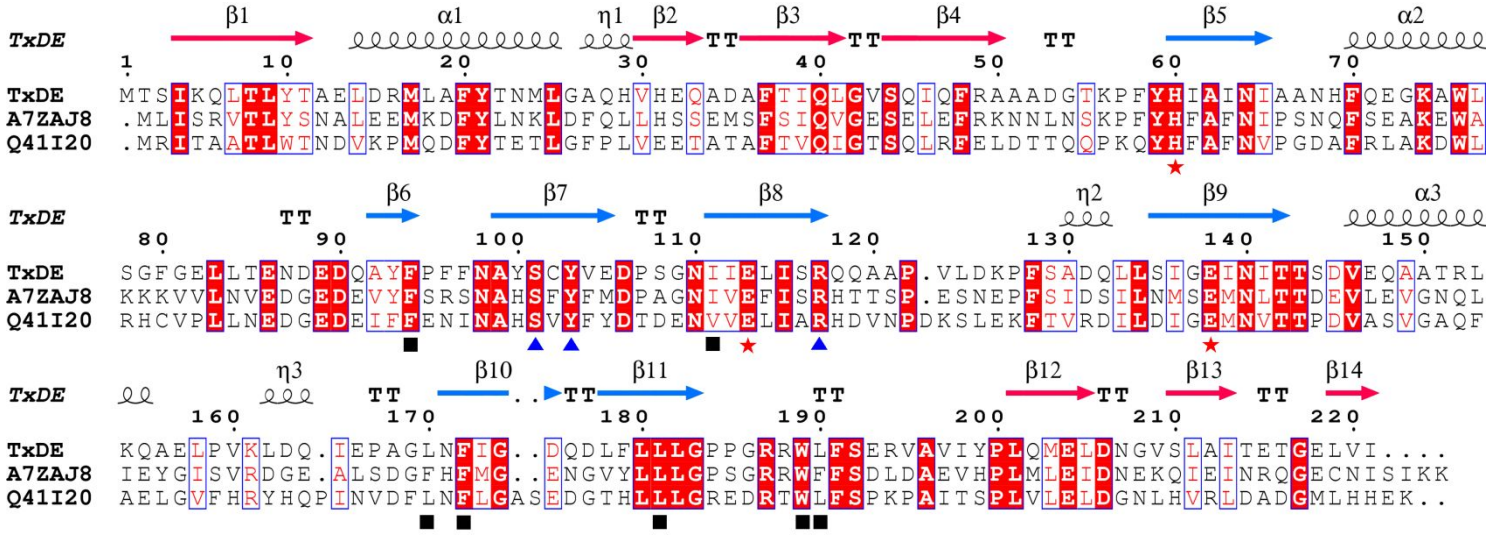
TxDE
β1 α1 η1 β2 β3 β4 β5 α2
TT TT TT
1 10 20 30 40 50 60 70
TxDE MTSIKQLTLYTAELDRMLAFYTNMLGAQHVHEQADAFTIQLGVSQIQFRAAADGTKPFYHIAINIAANHFQEGKAWL
A7ZAJ8 .MLISRVTLYSNALEEMKDFYLNKLDFQLLHSSEMSFSIQVGESELEFRKNNLNSKPFYHFAFNIPSNQFSEAKEWA
Q41I20 .MRITAATLWTNDVKPMQDFYTETLGFPLVEETATAFTVQIGTSQLRFELDTTQQPKQYHFAFNVPGDAFRLAKDWL
TxDE
β6 β7 β8 η2 β9 α3
TT TT
80 90 100 110 120 130 140 150
TxDE SGFGELLTENDEDQAYFPFFNAYSCYVEDPSGNIIELISRQQAAP.VLDKPFSADQLLSIGEINITTSDVEQAATRL
A7ZAJ8 KKKVVLNVEDGEDEVYFSRSNAHSFYFMDPAGNIVEFISRHTTSP.ESNEPFSIDSILNMSEMNLTTDEVLEVGNQL
Q41I20 RHCVPLLNEDGEDEIFFENINAHSVYFYDTDENVVELIARHDVNPDKSLEKFTVRDILDIGEMNVTTPDVASVGAQF
TxDE
η3 β10 β11 β12 β13 β14
TT TT TT TT TT
160 170 180 190 200 210 220
TxDE KQAELPVKLDQ.IEPAGLNFIG..DQDLFLLLGPPGRRWLFSERVAVIYPLQMELDNGVSLAITETGELVI....
A7ZAJ8 IEYGISVRDGE.ALSDGFHFMG..ENGVYLLLGPSGRRWFFSDLDAEVHPLMLEIDNEKQIEINRQGECNISIKK
Q41I20 AELGVFHRYHQPINVDFLNFLGASEDGTHLLLGREDRTWLFSPKPAITSPLVLELDGNLHVRLDADGMLHHEK..

Figure 25. Multiple sequence alignment of TxDE. The amino acid sequence of TxDE and similar proteins are compared: TxDE from *Paenibacillus polymyxa JH2* (GenBank accession number: GQ9218340) (Koh *et al*., 2010) and uncharacterized proteins from *Bacillus amyloliquefaciens* (A7ZAJ8) and *Exiguobacterium sibiricum* (B1YFD6). Highly conserved residues are shown in red and boxed in blue; strictly conserved residues are shown on a red background. Three residues that interact with Mn(II) in the active site are indicated by red asterisks; blue triangles represent the residues involved in hydrogen bonding at the active site; and black squares indicate residues having van der Waals interactions with toxoflavin. The secondary structural elements are shown for the corresponding sequences, with the A-domain in red and the B-domain in blue. This figure was prepared using ESPript (Gouet *et al*., 1999).

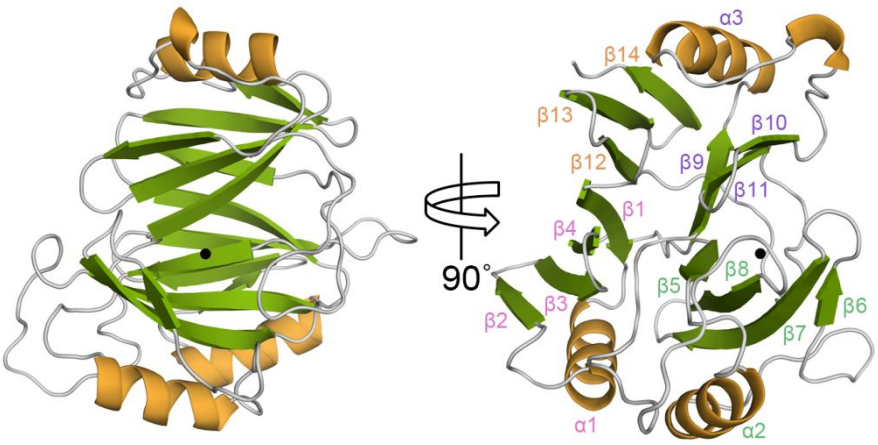

Figure 26. Overall structure of TxDE in the substrate-free form. A ribbon diagram is shown, with the corresponding secondary structures labeled as defined in Figure 25. The black sphere indicates the Mn(II) ion. In the left panel, the molecule is oriented to place the B-domain in front, and a different view is shown in the right panel. Labels for the secondary structures in each motif are indicated in different colors.

domain are almost orthogonal to each other, forming a highly concave surface along the seven-stranded β-sheet (Fig. 26). Helices α2 and α3 in the B-domain are positioned respectively at each end of the sheet.

2. Interactions between the two domains

The overall structure of TxDE is stabilized by interactions between the two domains. In particular, the two β-sheets are packed in a parallel manner, such that the side chains of β-strands in the A-domain interact closely with those in the B-domain. These interactions are mediated mainly by hydrophobic residues. Specifically, leucine and isoleucine residues are predominantly located at the interface between the two domains: β3, β4, β1, β12, β13 from the A-domain and β11, β9, β5, β8 from the B-domain (Fig. 27). These interactions are so hydrophobic and extensive that water molecules are not present between the two layers of β-sheets, with a total of 864 $Å^2$ of the buried surface area, corresponding to 26% of the surface area of each sheet. In addition, the three helices, located at both ends of the β-sheet, seal off the potential cavity in the interdomain interface (Fig. 27). Specifically, residues in α1 (Met17, Phe20, Met24, and Leu25) and in α2 (Trp76, Leu77, and Phe80) form hydrophobic interactions with residues in the A-domain (Phe37, Leu39, Leu41, and Phe48) and in the B-domain (Val104 and Leu114), along with a

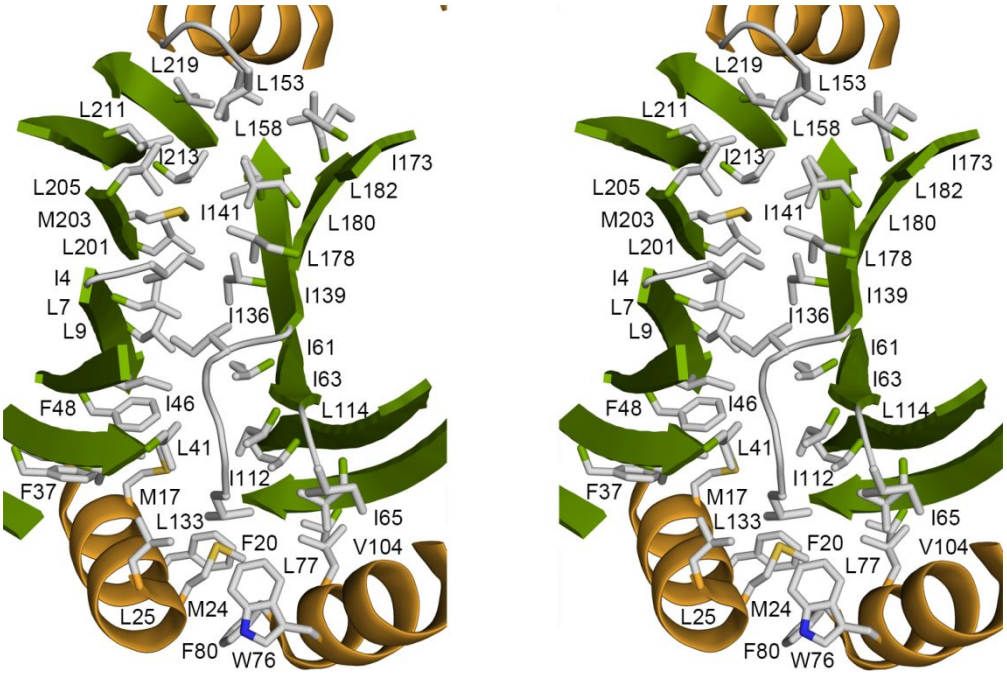

Figure 27. Stereoscopic view of interaction residues between two domains. Hydrophobic interactions between the A- and B-domains are shown. Hydrophobic residues such as leucine, isoleucine, and phenylalanine are predominantly located in this interdomain interface. These residues along the β-sheet include Ile213, Leu211, Leu205, Met203, Leu201, Ile4, Leu7, Leu9, Ile46, Phe48, and Leu41 from the A-domain, and Ile173, Leu178, Leu180, Leu182, Ile136, Ile139, Ile141, Ile61, Ile63, and Ile112 from the B-domain.

loop (Ile65 and Leu133) connecting the A- and B-domains. At the other end of the β-sheet, Leu153 from α3 participates in interactions with Leu219 of the A-domain, as well as Leu158, Ile173, and Leu182 of the B-domain. All of these residues are within 4 Å of each other.

3. Active site in the substrate-free TxDE

The location of the active site in TxDE was suggested by the presence of a possible metal binding site in the B-domain (Fig. 26), consistent with the requirement of a Mn(II) ion for its catalytic activity (Fig. 22) (Koh *et al*., 2010). It had been also noted that TxDE became stable and soluble in the presence of Mn(II) ions; therefore, Mn(II) was supplemented at the early stage of protein purification. The metal binding site is embedded in the hydrophobic cavity in the B-domain, which was generated by a deep, concave, funnel-like surface enclosed by the hydrophobic residues. Unlike that in the A-domain, the funnel-like space in the B-domain has two possible openings, one at each end of the long axis of the funnel; however, these openings are effectively sealed off by mainly hydrophobic residues, including Phe96, Phe97, Phe172, and Phe179 at one end, and Ile111, Arg187, Arg188, Trp189, and Leu190 at the other (Fig. 28A). Although the top and bottom of the funnel are mostly closed off, there is a vent on the side of the funnel that connects the surface of

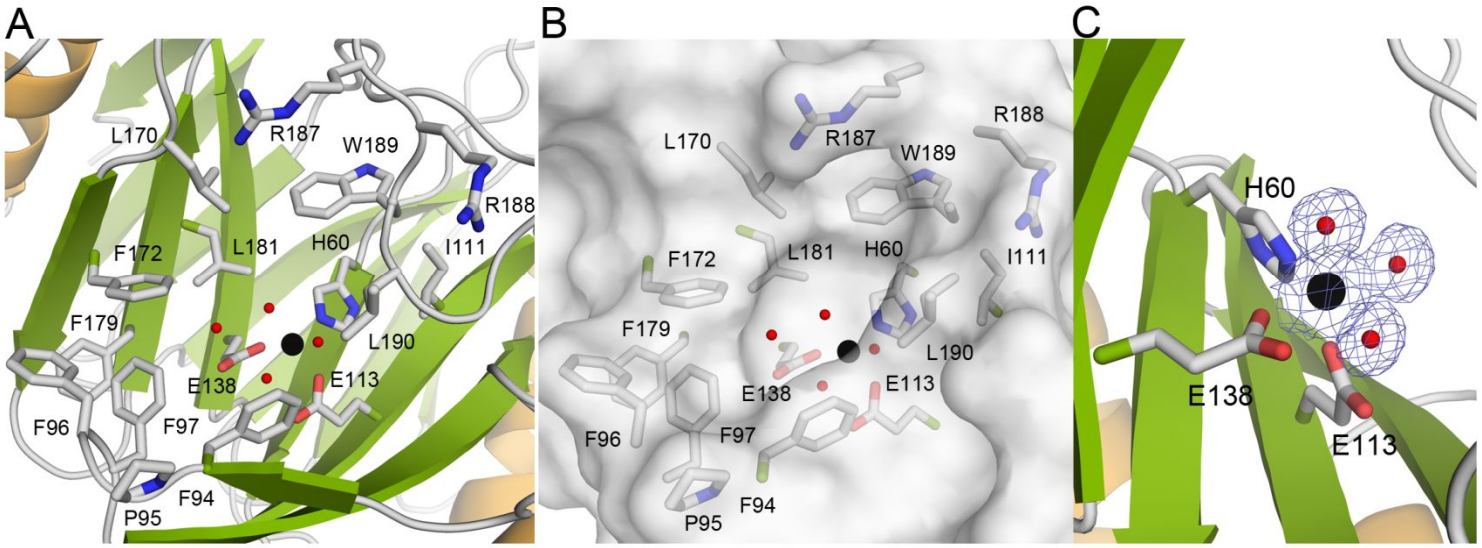
A
L170
R187
W189
R188
F172
L181
H60
I111
F179
L190
E138
E113
F96
F97
F94
P95
B
L170
R187
W189
R188
F172
L181
H60
I111
F179
L190
E138
E113
F96
F97
F94
P95
C
H60
E138
E113

Figure 28. The active site of TxDE in the substrate-free form. (A) A close-up view of the active site in the B-domain shows a deep, concave, funnel-like surface with nearby hydrophobic residues; the Mn(II)-binding site is indicated by the black sphere. (B) Surface representation of (A) shows that the metal binding site is located deep within a hydrophobic channel. (C) The active site metal has an octahedral coordination, with three amino acid ligands and three water molecules. The 2*Fo-Fc* electron density map contoured at 1σ clearly indicates the locations of the metal and the three water molecules, represented by black and red spheres, respectively.

the molecule to the inside of the enzyme (Fig. 28B). This channel is elliptical, with dimensions of 8610 Å on the basis of interatomic distance, and its wall is lined with hydrophobic residues: Phe94, Pro95, Phe96, Phe97, Ile111, Leu170, Phe172, Leu181, Trp189, and Leu190 (Fig. 28B). The metal binding site is located at the end of the 9 Å-long hydrophobic channel from the vent.

In the metal binding site, three residues from the inner wall of the funnel (His60 from β5, Glu113 from β8, and Glu138 from β9) as well as three well-ordered water molecules coordinate with the bound metal (Fig. 28C). These six ligands form a coordination shell of octahedral geometry, with an average distance of 2.2 Å to the bound metal (Table 5). In this coordination shell, His60 and Glu138 form part of the equatorial plane with two water molecules, each across from His60 and Glu138, respectively, while Glu113 and a water molecule *trans* to Glu113 serve as the axial ligand. In addition to these metal coordinating water molecules, there are several water molecules near the first coordination shell of the metal ion in the active site, within hydrogen bonding distance. The metal ion was identified as Mn(II) by the characteristic hyperfine signals from electron paramagnetic resonance spectroscopy (Fig. 29). Therefore, it was concluded that TxDE is a metalloenzyme requiring Mn(II) for its activity, and this is consistent with the

Table 5. Details for distances and angles (degrees) between a bound metal and its ligands.

(A) TxDE(D175A) in a substrate-free form

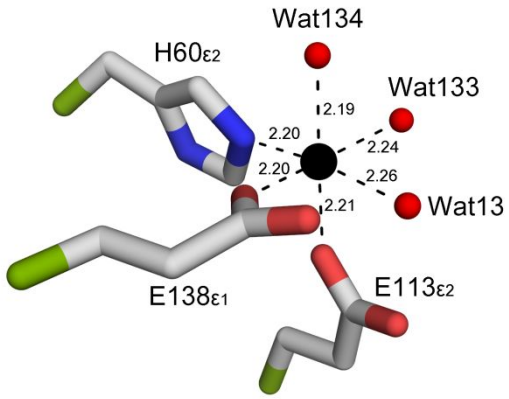

Defining Atoms	Observed Angles (degrees)	Defining Atoms	Observed Angles (degrees)
H60N$^{\varepsilon 2}$-Mn-E138O$^{\varepsilon 1}$	96.59	E113O$^{\varepsilon 2}$-Mn-Wat133	91.62
H60N$^{\varepsilon 2}$-Mn-Wat13	170.36	E138O$^{\varepsilon 1}$-Mn-E113O$^{\varepsilon 1}$	96.82
H60N$^{\varepsilon 2}$-Mn-Wat133	94.89	E138O$^{\varepsilon 1}$-Mn-Wat13	85.15
E113O$^{\varepsilon 1}$-Mn-Wat13	86.95	E138O$^{\varepsilon 1}$-Mn-Wat133	166.45
E113O$^{\varepsilon 1}$-Mn-H60N$^{\varepsilon 2}$	83.44	Wat133-Mn-Wat13	84.73
E113O$^{\varepsilon 1}$-Mn-Wat134	174.96	H60N$^{\varepsilon 2}$-Mn-Wat134	94.34
E138O$^{\varepsilon 1}$-Mn-Wat134	87.92	Wat133-Mn-Wat134	84.04
Wat13-Mn-Wat134	95.19		

(B) TxDE(D175A)-toxoflavin complex

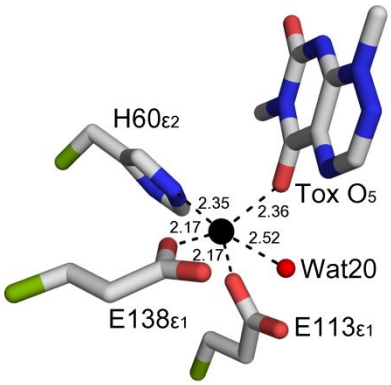

Defining Atoms	Observed Angles (degrees)	Defining Atoms	Observed Angles (degrees)
H60N$^{\varepsilon 2}$-Mn-E138O$^{\varepsilon 1}$	100.88	E113O$^{\varepsilon 2}$-Mn-Tox O5	88.14
H60N$^{\varepsilon 2}$-Mn-Wat20	171.34	E138O$^{\varepsilon 1}$-Mn-E113O$^{\varepsilon 1}$	121.48
H60N$^{\varepsilon 2}$-Mn-Tox O5	82.61	E138O$^{\varepsilon 1}$-Mn-Wat20	84.32
E113O$^{\varepsilon 1}$-Mn-Wat20	95.59	E138O$^{\varepsilon 1}$-Mn-Tox O5	150.15
E113O$^{\varepsilon 1}$-Mn-H60N$^{\varepsilon 2}$	87.63	Tox O1-Mn-Wat20	89.45

Wat20 in the complex is equivalent to Wat13 in a substrate-free TxDE.

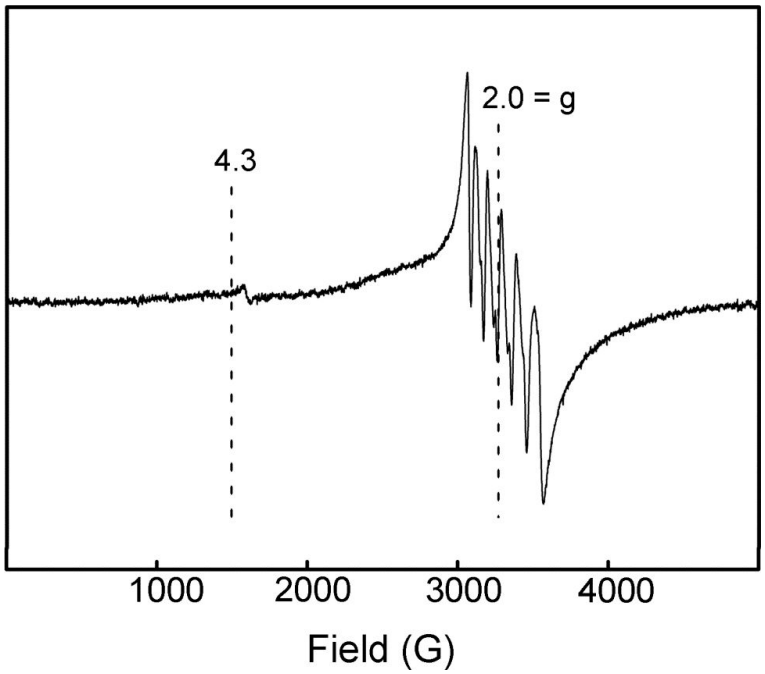

Figure 29. EPR spectrum of the purified TxDE. Sample contains 290 μM TxDE. EPR parameters: 100 K, 1-mW microwave power at 9.18 GHz, modulation amplitude 3.2 G.

results of a functional analysis (Fig. 22) (Koh *et al*., 2010).

4. Structural features of the TxDE–Toxoflavin complex

The structure of TxDE(D175A) in complex with toxoflavin, designated as TxDE(D175A)–Tox complex, was determined in a soaking experiment. Structural superposition of substrate-free TxDE(D175A) and its complex with toxoflavin, performed using the CCP4MG molecular graphics program (Collaborative Computational Project Number 4, 1994), did not indicate any noticeable differences in conformation between the two forms, which had a root mean square deviation of 0.33 Å for all Cα atoms.

Figure 30 shows the details of the active site in the TxDE(D175A)–Tox complex. The substrate toxoflavin is bound to the Mn(II)-coordination shell, with an orientation such that the planar ring of toxoflavin fits into the long axis of the elliptical channel, and the methyl group at N-1 points toward a vent (Fig. 30A and B). The binding site is surrounded by mainly hydrophobic residues in the wall of the channel: Phe94, Phe97, Ile111, Leu170, Phe172, Leu181, Trp189, and Leu190. Specifically, O5 of toxoflavin replaced the Mn(II)-ligating water molecule across from Glu138 of the equatorial plane in the substrate-free structure, at a distance of 2.4 Å relative to the Mn(II) ion, whereas another equatorial water molecule *trans* to His-60 remained in the

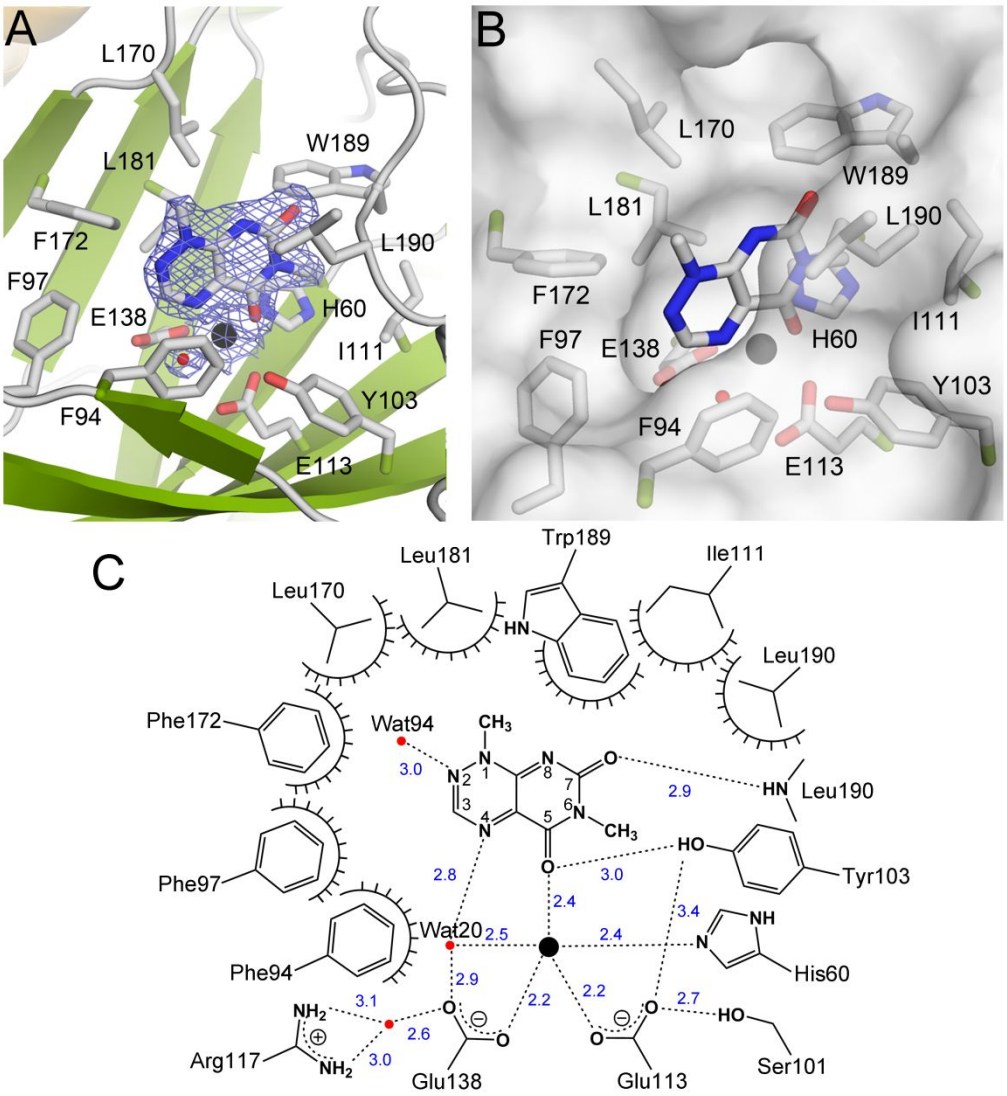
A
L170
W189
L181
F172
L190
F97
E138
H60
I111
Y103
F94
E113
B
L170
W189
L181
L190
F172
F97
E138
H60
I111
Y103
F94
E113
C
Trp189
Leu181
Ile111
Leu170
HN
Leu190
Phe172
Wat94
CH3
3.0
N
O
2.9
HN
Leu190
CH3
HO
Phe97
2.8
3.0
Tyr103
2.4
3.4
NH
Wat20
2.5
2.4
Phe94
His60
2.9
3.1
2.2
2.2
2.7
NH2
2.6
HO
Arg117
3.0
Glu138
Glu113
Ser101

Figure 30. The active site in the TxDE–Tox complex. (A) The binding of toxoflavin at the active site is shown, with the 2*Fo-Fc* electron density map contoured at 1σ for a bound Mn(II) ion (black sphere), water molecule (red sphere), and toxoflavin molecule. (B) The surface representation of the active site provides a better view of the toxoflavin molecule in the hydrophobic channel. (C) Schematic diagram showing the binding mode of toxoflavin in the active site. The dashed lines indicate putative hydrogen bonds, which are labeled with the interatomic distance (in Å); the decorated arcs represent van der Waals interactions of less than 5.0 Å. Water molecules and a bound Mn(II) ion are shown as red and black spheres, respectively.

coordination shell (Fig. 30A and Fig. 31). However, the axial water molecule, which was present in the substrate-free form, was absent in the active site of the complex. The planar ring of toxoflavin was at an angle of about 55° relative to the equatorial plane of the coordination shell; thus the axial ligand, if present, would have been only about 2.8 Å from the toxoflavin ring (Fig. 31). Other water molecules present in the substrate-free form were also replaced; in particular, the methyl groups at N-6 and O-7 now occupy the positions of water molecules in the substrate-free form.

The binding of toxoflavin in the complex appears to be stabilized by hydrophobic interactions and hydrogen bonds (Fig. 30A and C). Specifically, the side chains of Phe94, Phe172, Trp189, and Leu190 are within 4.0 Å of toxoflavin, with the side chains of Phe94 and Leu190 positioned parallel to the toxoflavin ring at a distance of 3.6–3.8 Å (Fig. 30A and Fig. 31). Other hydrophobic residues such as Phe97, Leu170, and Leu181 are involved in the formation of a hydrophobic environment over a range of 4–5 Å from toxoflavin. In addition to these hydrophobic interactions, there are several hydrogen bonds between toxoflavin and its neighboring residues: O-5 to the hydroxyl group of Tyr103 at 3.0 Å, O-7 to the main chain nitrogen of Leu190 at 2.9 Å, and N-2 to a water molecule at 3.0 Å. It is noteworthy that the side chains of Trp189 and Leu190 are oriented such that part of the toxoflavin is

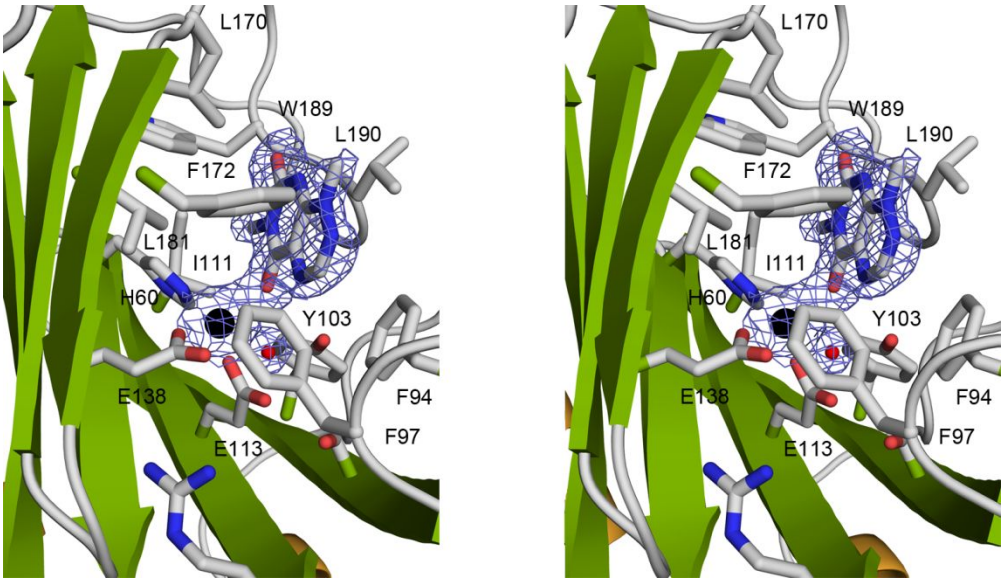

Figure 31. Stereoscopic view of the active site of the TxDE–Toxoflavin complex. This view, obtained by a rotation of about 90° along the vertical axis of Figure 30A, illustrates that the possible sixth coordinating ligand is missing in this complex. The electron density of 2*Fo-Fc* contoured at 1σ is shown for a bound Mn(II) (black sphere), water molecule (red sphere), and toxoflavin molecule.

sandwiched into the cavity between these two side chains (Fig. 30A and Fig. 31). This binding mode is likely to be stabilized by hydrophobic interactions and a hydrogen bond between O-7 and the main-chain nitrogen of Leu190, as described above.

5. Functional analysis

To understand the functional roles of residues in the active site, thin-layer chromatographic analysis was performed to measure the degradation of toxoflavin after reaction with various mutant enzymes. In fact, the kinetic parameters of the wild-type and each mutant enzyme were unsuccessful to measure using UV-Visible spectroscopic and thin-layer chromatographic analysis, mainly due to the complexity of the reaction (see *Discussion*), as well as the detection limits of thin-layer chromatographic analysis.

First, it was examined whether TxDE catalyzes toxoflavin degradation in an oxygen-dependent manner, because it was indicated that TxDE is structurally similar to oxygen-dependent enzymes by these analysis (see *Discussion*). The assay results indicated that substantial amounts of toxoflavin remained under anaerobic conditions, in contrast to aerobic conditions (Fig. 32), strongly supporting the suggestion that TxDE requires oxygen, as well as Mn^{2+} and the reducing agent DTT, for the degradation of toxoflavin (Fig. 22)

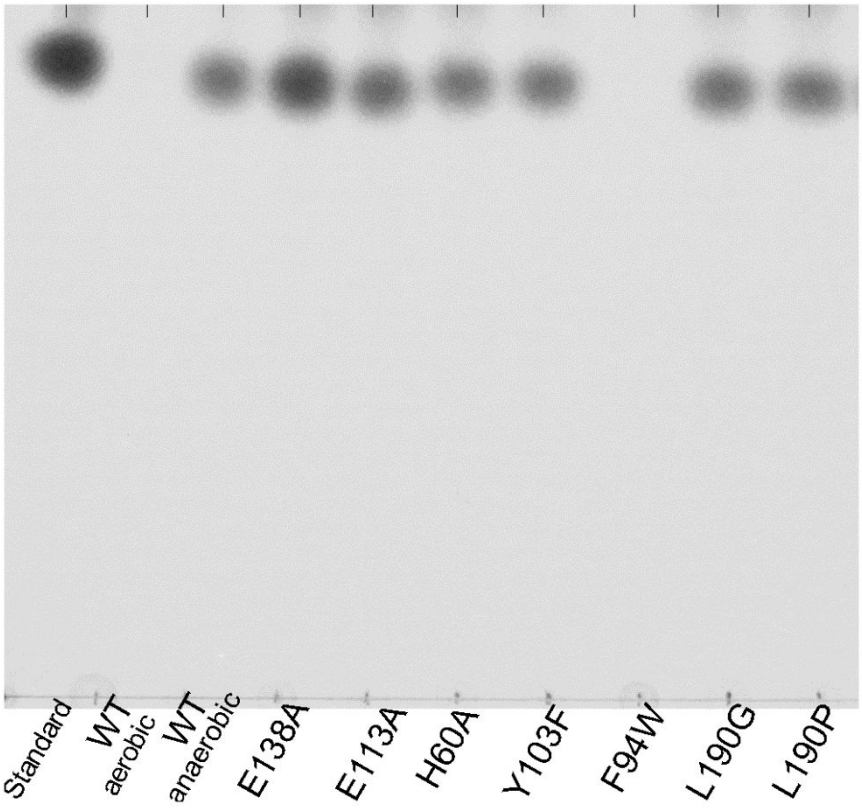
Standard
WT aerobic
WT anaerobic
E138A
E113A
H60A
Y103F
F94W
L190G
L190P

Figure 32. Thin-layer chromatographic analysis of toxoflavin degradation under various conditions using wild-type and mutant TxDEs. Reactions were performed at 25°C under aerobic conditions, unless specified. Chemically synthesized toxoflavin is shown as the Standard. The wild-type enzyme was highly inactive under anaerobic conditions. Enzymes with mutations of the metal-binding residues E138A, E113A, or H60A or of other residues near the active site (Y103F, L190G, or L190P) were catalytically incompetent relative to the wild-type enzyme. Note that some variations of intensity for the residual toxoflavin after a reaction are mainly due to the recovery yield, while chemically synthesized toxoflavin was used as a standard without a reaction.

(Koh *et al*., 2010). Second, the residues in the Mn(II)-binding site (Fig. 28C) were also shown to be essential for the catalytic activity of the enzyme (Fig. 32), consistent with the metal requirement for enzyme activity. In addition, it was shown that the hydroxyl group of Tyr103 and the hydrophobic features of Leu190 and Phe94 play a crucial role in enzyme catalysis.

DISCUSSION

Low molecular weight toxins secreted from pathogenic bacteria exert destructive effects as virulence factors in various hosts; the modes of action for fungal toxins have been reviewed (Möbius and Hertweck, 2009). The identification of enzymes capable of degrading these toxins may provide an alternative antivirulence strategy for toxin-mediated diseases. To facilitate the investigation of the catalytic features of toxoflavin-degrading enzyme, the crystal structure of TxDE from *P. polymyxa JH2* is reported in this paper. This enzyme exhibits *in vitro* degradation activity toward phytotoxin toxoflavin, a virulence factor produced by the pathogenic bacterium *B. glumae* (Kim *et al*., 2004; Koh *et al*., 2010). Structural analysis of the substrate-free form of TxDE and its complex with the substrate toxoflavin, as well as the results of a functional analysis, suggest the unique features of the enzyme.

TxDE appears to be novel in its *in vitro* function, as no other enzymes with a similar function have been characterized to date; however, hypothetical proteins with sequence similarities of 52–57% with TxDE were identified from various *Bacillus* species (37% identity and 57% similarity) and *Exiguobacterium sibiricum* (38% identity and 52% similarity), which were annotated as members of the glyoxalase family (Fig. 25) (see below). A

structural alignment search using DALI (Holm and Sander, 1998) indicated that TxDE is structurally similar to a functionally uncharacterized protein from *B. cereus* (Z-score, 12.2; sequence identity, 11%; PDB ID 1ZSW from Midwest Center for Structural Genomics) and has limited structural similarity with other functionally known proteins, despite a low degree of sequence similarity (6–25%) and low Z-score (4.8–8.6). In fact, all of these structurally similar proteins are members of the vicinal oxygen chelate superfamily of metalloenzymes (Bergdoll *et al*., 1998; Armstrong, 2000), which includes glyoxalase, bleomycin resistance protein, fosfomycin resistance protein, methylmalonyl-coenzyme A epimerase, and bacterial extradiol dioxygenases. Proteins in this family share a common structural feature in which the βαββββ motif is the basic structural module of their three-dimensional conformation, although the numbers and relative orientations of these modules in the monomer and their oligomerization vary among the proteins (Bergdoll *et al*., 1998; Armstrong, 2000). Specifically, glyoxalase and bleomycin resistance protein in this family contain two βαββββ motifs in each monomer and form a functional dimer; the edge-to-edge interactions of β-strands between motifs in different monomers generate two independent active sites at the intersubunit interface (Fig. 33A). In contrast, 2,3-dihyroxybiphenyl 1,2-dioxygenase (DHBD) from *Pseudomonas cepacia* (Han *et al*., 1995) is similar to TxDE in

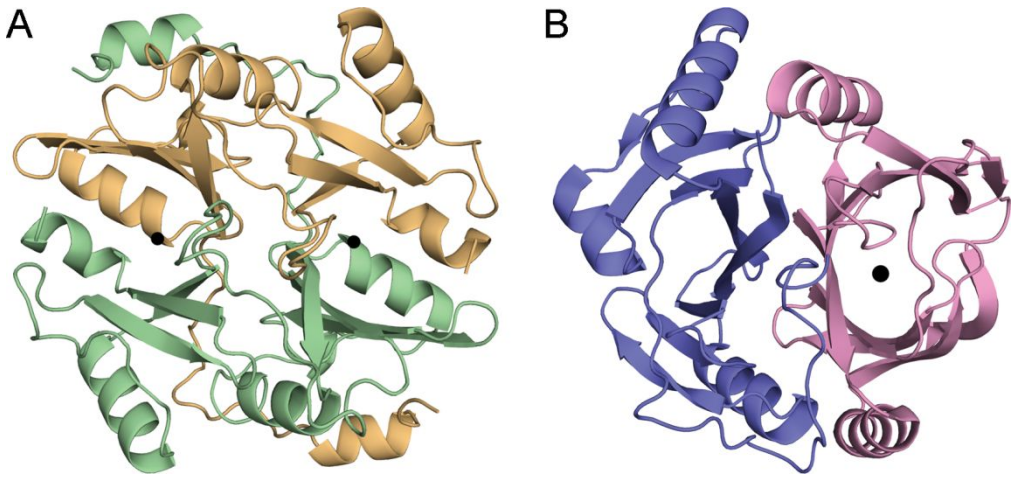

Figure 33. Overall structure of glyoxalase and 2,3-dihyroxybiphenyl 1,2-dioxygenase (DHBD). (A) As described in the text, a dimer of glyoxalase (PDB ID 1FRO) (Cameron *et al.*, 1997) generates two independent active sites at the intersubunit interface. Each monomer is indicated in a different color, and the active sites are presented with a bound metal ion (black sphere). (B) The structure of monomeric DHBD (PDB ID 1HAN) (Han *et al.*, 1995) was similar to that of TxDE in this study. Each domain is colored differently. In each domain, two sequentially ordered βαβββ motifs form continuous β-stands by edge-to-edge interactions. The C-terminal active site is shown with a bound metal ion (black sphere).

that there are four motifs in the monomer, with sequentially ordered motifs mediating edge-to-edge interactions and forming two domains, and the active site is present in only one particular domain (Fig. 33B). From a structural perspective, the topology of TxDE differs from that of the three proteins described above; four motifs in the monomer that form a continuous β-stand in two domains are not assembled in a sequential manner, but rather with edge-to-edge interactions between motifs 1 and 4, and motifs 2 and 3 (Fig. 26).

The structural similarity with DHBD is extended to the active site of TxDE, in which one histidine and two glutamate residues along with three water molecules serve as the first coordination shell for Mn(II) (Fig. 28C and Table 5). In the extradiol dioxygenases, to which DHBD belongs, two histidines and one carboxylate with three water molecules is a common motif of the active site bearing Fe(II) or Mn(II), to catalyze ring cleavage of catecholic compounds by activating and incorporating dioxygen into the substrate, producing a ring-opened product (Vaillancourt *et al.*, 2006; Kovaleva and Lipscomb, 2008). Consistent with this structural similarity, mutation of the Mn(II)-coordinating residues His60, Glu113, and Glu138 (Fig. 32), as well as the absence of Mn(II) from the reaction medium, abolished TxDE enzyme activity (Fig. 22). It was also noticed that in contrast to aerobic conditions, the substrate toxoflavin was not efficiently degraded under

anaerobic conditions (Fig. 32). Taken together, these observations suggest that TxDE catalyzes the degradation of toxoflavin in an oxygen- and Mn(II)-dependent manner.

This functional analysis also indicates that the identity and precise orientation of active site residues play an essential role in catalysis, possibly by positioning the incoming toxoflavin into the productive binding mode for catalysis. Consistent with the structural implication of Phe94 (Fig. 30A), the F94W mutant enzyme, which could enhance stacking interactions with the substrate, maintained activity, whereas the F94S mutant was catalytically inactive (Fig. 32 and Fig. 22). Also, the absence of a hydrophobic feature in the L190G mutant and a possible distortion of the main chain in the L190P mutant almost abolished enzyme activity (Fig. 32), supporting the proposed structural role of Leu190 as a part of the substrate binding pocket (Fig. 30). The functional role of the hydroxyl group in Tyr103 remains to be established.

Another notable feature of TxDE is the requirement for the reducing agent DTT for catalysis (Fig. 22) (Koh *et al.*, 2010). The results of UV-visible spectroscopic analysis suggested that toxoflavin is subject to chemical modification by DTT, even in the absence of the enzyme, to form reduced toxoflavin (peak at 244 nm) and oxidized DTT (i.e., 1,2-dithiane-4,5-diol; peak at 287 nm) (Fig. 23). Subsequent NMR experiments also validated that

toxoflavin is converted to 4,8-dihydrotoxoflavin in the presence of DTT, with the concurrent formation of oxidized DTT (Fig. 24). Further analysis indicated that the reduced form of toxoflavin indeed serves as a substrate for the enzyme (Fig. 23).

Therefore, DTT is a prerequisite for the formation of the reduced form of toxoflavin. An unusual feature of TxDE-dependent catalysis is the reaction product(s). In a dioxygenase-catalyzed reaction, the product is a chemically stable muconic semialdehyde adduct (Vaillancourt *et al*., 2006; Kovaleva and Lipscomb, 2008). However, there is no solid evidence for the stable products from TxDE-dependent degradation of toxoflavin; instead, many molecules with a diverse range of molecular mass, but lower than that of toxoflavin, were characterized by LC-MS analysis. This strongly suggests that TxDE produces a chemically labile molecule which cannot be characterized under this LC-MS analysis, and the unstable molecule(s) is likely subject to successive reactions in a spontaneous or/and enzyme-dependent manner. In fact, the reduced form of toxoflavin, not the oxidized form, was shown to be subject to oxidation and decarboxylation (Nagamatsu *et al*., 2009; Müller, 1987). Therefore, it is postulated that toxoflavin is reduced by DTT and subsequently 4,8-dihydrotoxoflavin is subject to oxidation for further reaction which is not yet characterized. Owing to the complexity of the TxDE reaction, the detailed

features with regard to the catalytic mechanism and final product by TxDE remain to be elucidated. Further investigations are required to answer details of the degradation pathway.

In this study, it was determined that the crystal structure of TxDE, an enzyme that exhibits *in vitro* degradation activity against the phytotoxin toxoflavin. Structural and functional analyses indicate that the enzyme is similar to a dioxygenase in both its structure and function, and that toxoflavin degradation is catalyzed in an oxygen-, DTT-, and Mn(II)-dependent manner. The characterization of TxDE may facilitate the development of disease-resistant crop plants as well as applications in other areas of biotechnology (Koh *et al*., 2010).

REFERENCES

Armstrong, R. N. (2000) Mechanistic diversity in a metalloenzyme superfamily. *Biochemistry* **39**: 13625–13632.

Agrios, G. N. (2005) How pathogens attack plants. In: Agrios, G. N., ed. *Plant Pathology* (5th edition). Elsevier: Academic Press. 190–196.

Bergdoll, M., Eltis, L. D., Cameron, A. D., Dumas, P., and Bolin, J. T. (1998) All in the family: Structural and evolutionary relationships among three modular proteins with diverse functions and variable assembly. *Protein Sci.* **7**: 1661–1670.

Block, A., Li, G., Fu, Z. Q., and Alfano, J. R. (2008) Phytopathogen type III effector weaponry and their plant targets. *Curr. Opin. Plant Biol.* **11**: 396–403.

Bokhove, M., Nadal Jimenez, P., Quax, W. J., and Dijkstra, B. W. (2010) The quorumquenching *N*-acyl homoserine lactone acylase PvdQ is an Ntn-hydrolase with an unusual substrate-binding pocket. *Proc. Natl. Acad. Sci.* USA **107**: 686–691.

Brunger, A. T., Adams, P. D., Clore, G. M., DeLano, W. L., Gros, P., Grosse-Kunstleve, R. W., Jiang, J. S., Kuszewski, J., Nilgus, M., Pannu, N. S., Read, R. J., Rice, L. M., Simonson, T., and Warren, G. L. (1998) Crystallography

& NMR System: A new software suite for macromolecular structure determination. *Acta Crystallogr. Sect. D Biol. Crystallogr.* **54**, 905-921.

Cameron, A. D., Olin, B., Ridderstrom, M., Mannervik, B., and Jones, T. A. (1997) Crystal structure of human glyoxalase I—evidence for gene duplication and 3D domain swapping. *EMBO J.* **16**: 3386–3395.

Chisholm, S. T., Coaker, G., Day, B., and Staskawicz, B. J. (2006) Host-microbe interactions: Shaping the evolution of the plant immune response. *Cell* **124**: 803–814.

Choi, G., Lee, J., Ji, J. Y., Woo, J., Kang, N. S., Cho, S. Y., Kim, H. R., Ha, J. D., and Han, S. Y. (2013) Discovery of a potent small molecule SIRT1/2 inhibitor with anticancer effects. *Int. J. Oncol*. **43**, 1205–1211.

Collaborative Computational Project, Number 4 (1994) The CCP4 suite: programs for protein crystallography. *Acta Crystallogr. Sect. D Biol. Crystallogr.* **50**: 760–763.

Dong, Y. H., Wang, L. Y., and Zhang, L. H. (2007) Quorum-quenching microbial infections: mechanisms and implications. *Phil. Trans. R. Soc. B* **362**: 1201–1211.

Dong, Y. H., Wang, L. H., Xu, J. L., Zhang, H. B., Zhang, X. F., and Zhang, L. H. (2001) Quenching quorum-sensing-dependent bacterial infection by an *N*-acyl homoserine lactonases. *Nature* **411**: 813–817.

Fenwick, M. K., Philmus, B., Begley, T. P., and Ealick, S. E. (2011) Toxoflavin lyase requires a novel 1-His-2-carboxylate facial triad. *Biochemistry* **50**: 1091–1100.

Gala´n, J. E. (2009) Common themes in the design and function of bacterial effectors. *Cell Host Microbe* **5**: 571–579.

Gouet, P., Courcelle, E., Stuart, D. I., and Me´toz, F. (1999) ESPript: Analysis of multiple sequence alignments in PostScript. *Bioinformatics* **15**: 305–308.

Han, S., Eltis, L. D., Timmis, K. N., Muchmore, S. W., and Bolin, J. T. (1995) Crystal structure of the biphenyl-cleaving extradiol dioxygenase from a PCB-degrading pseudomonad. *Science* **270**: 976–980.

Holm, L., and Sander, C. (1998) Touring protein fold space with Dali/FSSP. *Nucleic Acids Res.* **26**: 316–319.

Jones, T. A., Zou, J. Y., Cowan, S. W., and Kjeldgaard, M. (1991) Improved methods for building protein models in electron density maps and the location of errors in these models. *Acta Crystallogr. Sect. A* **47**: 110–119.

Kim, J., Kim, J. G., Kang, Y., Jang, J. Y., Jog, G. J., Lim, J. Y., Kim, S., Suga, H., Nagamatsu, T., and Hwang, I. (2004) Quorum sensing and the LysR-type transcriptional activator ToxR regulate toxoflavin biosynthesis and transport in *Burkholderia glumae*. *Mol. Microbiol.* **54**: 921–934.

Koh, S., Kim, H., Kim, J., Goo, E., Kim, Y. J., Choi, O., Jwa, N. S., Ma, J., Nagamatsu, T., Moon, J. S., and Hwang, I. (2010) A novel light-dependent selection marker system in plants. *Plant Biotechnol. J.* **9**: 348–358.

Kovaleva, E. G., and Lipscomb, J. D. (2008) Versatility of biological non-heme Fe(II) centers in oxygen activation reactions. *Nat. Chem. Biol.* **4**: 186–193.

Latuasan, H. E., and Berends, W. (1961) On the origin of the toxicity of toxoflavin. *Biochim. Biophys. Acta* **52**: 502–508.

Lee, S. H., and Kohn, H. (2003) Phosphine-assisted rearrangement of 4,5-dihydroxy-1,2-dithianes to 4-hydroxy-3-mercaptotetrahydrothiophenes. *Heterocycles* **60**: 47–56.

Meiss, E., Konno, H., Groth, G., and Hisabori, T. (2008) Molecular processes of inhibition and stimulation of ATP synthase caused by the phytotoxin tentoxin. *J. Biol. Chem.* **283**: 24548–24553.

Möbius, N., and Hertweck, C. (2009) Fungal phytotoxins as mediators of virulence. *Curr. Opin. Plant Biol.* **12**: 390–398.

Mudgett, M. B. (2005) New insights to the function of phytopathogenic bacterial type III effectors in plants. *Annu. Rev. Plant Biol.* **56**: 509–531.

Müller, F. (1987) Flavin radicals: chemistry and biochemistry. *Free Radical Biol. Med.* **3**: 215–230.

Nagamatsu, T., Hashiguchi, Y., Sakuma, Y., and Yoneda, F. (1982) Autocycling oxidation of amines to carbonyl compound catalized by 3,4-disubstituted 4-deazatoxoflavin derivatives. *Chemistry Lett.* **11**: 1309–1312.

Nagamatsu, T. (2001) Syntheses, transformation, and biological activities of 7-azapteridine antibiotics: toxoflavin, fervenulin, reumycin and their analogs. *Recent Res. Devel. Org. Bioorg. Chem.* **4**: 97–121.

Nagamatsu, T., Ma, J., and Yoneda, F. (2009) The facile synthesis of 6-azapurines by transformation of toxoflavins (7-azapteridines). *Heterocycles* **77**: 849–854.

Otwinowski, Z., and Minor, W. (1997) Processing of X-ray diffraction data collected in oscillation mode. *Methods Enzymol.* **267**: 307–326.

Raoof, A., Depledge, P., Hamilton, N. M., Hamilton, N. S., Hitchin, J. R., Hopkins, G. V., Jordan, A. M., Maguire, L. A., McGonagle, A. E., Mould, D. P., Rushbrooke, M., Small, H. F., Smith, K. M., Thomson, G. J., Turlais, F., Waddell, I. D., Waszkowycz, B., Watson, A. J., and Ogilvie, D. J. (2013) Toxoflavins and deazaflavins as the first reported selective small molecule inhibitors of tyrosyl-DNA phosphodiesterase II. *J. Med. Chem.* **56**, 6352–6370.

Schuster, M., and Greenberg, E. P. (2006) A network of networks: Quorum-sensing gene regulation in *Pseudomonas aeruginosa*. *Int. J. Med. Microbiol.* **296**: 73–81.

Terwilliger, T. C., and Berendzen, J. (1999) Automated MAD and MIR structure solution. *Acta Crystallogr. Sect. D* **55**: 849–861.

Terwilliger, T. C. (2000) Maximum-likelihood density modification. *Acta Crystallogr. Sect. D* **56**: 965–972.

Trinchieri, G., and Sher, A. (2007) Cooperation of Toll-like receptor signals in innate immune defense. *Nat. Rev. Immunol.* **7**: 179–190.

Vaillancourt, F. H., Bolin, J. T., and Eltis, L. D. (2006) The ins and outs of ring-cleaving dioxygenases. *Crit. Rev. Biochem. Mol. Biol.* **41**: 241–267.

Wurtele, M., Jelich-Ottmann, C., Wittinghofer, A., and Oecking, C. (2003) Structural view of a fungal toxin acting on a 14-3-3 regulatory complex. *EMBO J.* **22**: 987–994.

Yoneda, F., and Nagamatsu, T. (1973) Tranformation of toxoflavin into fervenulin *via* 1-demethyltoxoflavin. *Tetrahydron Lett*. **17**: 1577–1580.

This paper was published in PLoS ONE in 2011 under the same title. Jung, W. S., Lee, J., Kim, M. I., Ma, J., Nagamatsu, T., Goo, E., Kim, H., Hwang, I., Han, J., and Rhee, S. (2011) Structural and functional analysis of phytotoxin toxoflavin-degrading enzyme. *PLoS ONE* 6, e22443.

ABSTRACT IN KOREAN

이눌린 분해효소인 Inulin Fructotransferase (IFTase)는 글리코시드 가수분해효소군 (glycoside hydrolase family) 91에 속하며, 분자내 프락토실 전이 (intramolecular fructosyl transfer)를 거쳐 고리 무수물 (cyclic anhydride)로서 말단의 디프락토당 단위로 연속으로 제거하여 베타-2,1-프룩탄 (β-2,1-fructan)을 해중합 (depolymerization) 하는 효소이다. 이눌린 분해효소의 결정 구조와 기질과 결합한 복합 구조에서 동일하게 IFTase는 삼량체 (trimer)로 구성된 효소로 나타난다. 그리고 각각의 단량체 (monomer)는 시계방향 병렬 베타-나선 구조 (right-handed β-helix)로 구성되어 있다. 비록 베타-사슬의 개수와 형태는 다양하지만, IFTase의 베타-나선은 다른 베타-나선 구조를 주로 연상시키는 구조를 가지고 있다. 그러나, 삼량체 형태가 효소 활성을 위한 전제 조건이라는 것과 활성 부위가 단량체와 단량체의 접점 (interface)에 위치해 있다는 것은 기존에 알려진 베타-나선 구조에서는 전례가 없었다. 결정학적 연구와 위치선택적 돌연변이 (site-directed mutagenesis)를 통한 연구 결과로부터 IFTase가 말단 용해 형태 (exolytic-type)의 활성을 갖는다는 구조적 토대를

마련하였고, 역전 형태 (inverting-type)의 글리코실 전이효소 (glycosyl transferase)라는 기능적 유사성도 밝혔다.

병원성 박테리아는 다양한 기주에서 박테리아의 병원성에 중요한 역할을 하는 발병 요인으로서, 유독성의 작은 분자량의 화합물을 합성하고 세포 밖으로 분비한다. 그러므로, 이들 화합물은 병원성에 대항하기 위한 목표가 된다. 식물병원균인 *Burkholderia glumae* BGR1은 세균성 벼알마름병과 농작물의 세균성 마름병을 유발하는 식물 독소인 톡소플라빈 (toxoflavin)을 생산한다. 최근에는 토양 미생물인 *Paenibacillus polymyxa* JH2로부터 톡소플라빈을 분해하는 효소 (TxDE)를 발견하였다. TxDE의 결정 구조는 기질이 결합하지 않은 형태는 1.6Å의 해상도, 톡소플라빈이 결합된 형태는 2.0Å의 해상도로 생화학적 기능 분석 결과와 함께 구명하였다. TxDE의 전체 구조는 아미노산 서열이 상이하나 인접 산소 킬레이트 금속 효소군 (vicinal oxygen chelate superfamily of metalloenzymes)의 3차 구조와 매우 유사하였다. 이 효소의 활성 부위는 소수성 홈의 끝부분에 9Å의 길이로 위치하고 있으며, 한 개의 히스티딘 (histidine)잔기, 두 개의 글루타메이트 (glutamate)잔기, 그리고 3개의 물 분자가 팔면체 배위 (octahedral coordination)로 결합된 2가 망간

(Mn(II)) 이온이 활성 부위에 존재한다. 기질이 결합된 효소는 구조적으로 유사하지만, 톡소플라빈이 기존의 2가 망간의 배위 전자층에 결합하고 있는 물 분자를 대신해 결합한다. TxDE는 효소의 생화학적 연구 결과에서 산소, 2가 망간 이온, 그리고 환원제인 디티오트레이톨 (dithiothreitol)에 의존하여 톡소플라빈의 분해를 촉매하였다. 이 결과들은 TxDE의 촉매 반응 원리를 밝히는 토대를 제공하였고, TxDE가 식물 유전공학에서 비항생제 선발 마커 (non-antibiotic selection marker)로서의 기능과 톡소플라빈에 의한 식물병에서 항병원성 인자 (antivirulence factor)로서의 기능을 연구하는 기초를 마련하였다.

주요어 : 결정 구조, 프룩탄, 이눌린 분해효소, 디프룩토스 무수물, 시계방향 병렬 베타 나선구조, 역전 형태 글루코실 전이효소, 식물 독소, *Burkholderia glumae*, *Paenibacillus polymyxa* JH2, 톡소플라빈 분해 효소, βαβββ-모티프, 금속 효소

학 번 : 2004-31068

CURRICULUM VITAE

Name: Jung, Woo-Suk

Sex: Male

Date of Birth: June 19, 1976

Date of Birth: Seoul, South Korea

Present Address: Functional Food Center, Gangneung Institute

Korea Institute of Science and Technology

Gangwon-do, 210-340, South Korea

Phone: +82-33-650-3690

Fax: +82-33-650-3679

E-mail: woosukjung@kist.re.kr

Education: Seoul National University, Seoul, South Korea

B.S. in Applied Biology and Chemistry (2002)

Seoul National University, Seoul, South Korea

M.S. in Agricultural Biotechnology (2004)

Seoul National University, Seoul, South Korea

Ph.D. in Agricultural Biotechnology (2014)

PUBLICATIONS

Jung, W. S., Hong, C. K., Lee, S., Kim, C. S., Kim, S. J., Kim, S. I., and Rhee, S. (2007) Structural and functional insights into intramolecular fructosyl transfer by inulin fructotransferase. *J. Biol. Chem*. **282**, 8414–8423.

Jung, W. S., Lee, J., Kim, M. I., Ma, J., Nagamatsu, T., Goo, E., Kim, H., Hwang, I., Han, J., and Rhee, S. (2011) Structural and functional analysis of phytotoxin toxoflavin-degrading enzyme. *PLoS ONE* **6**, e22443.

Jung, W. S., Singh, R. K., Lee, J. K., and Pan, C. H. (2013) Crystal structure and substrate specificity of $_D$-galactose-6-phosphate isomerase complexed with substrates. *PLoS ONE* **8**, e72902.